

STELLAR STREAM AND HALO STRUCTURE IN THE ANDROMEDA GALAXY FROM A SUBARU/HYPER SUPRIME-CAM SURVEY¹

YUTAKA KOMIYAMA^{2,3}, MASASHI CHIBA⁴, MIKITO TANAKA⁵, MASAYUKI TANAKA², TAKANOBU KIRIHARA^{6,7},
YOHEI MIKI^{8,9,10}, MASAO MORI^{6,8}, ROBERT H. LUPTON¹¹, PURAGRA GUHATHAKURTA¹², JASON S. KALIRAI^{13,14},
KAROLINE GILBERT^{13,14}, EVAN KIRBY¹⁵, MYUN GYOON LEE¹⁶, IN SUNG JANG¹⁶, SANJIB SHARMA¹⁷, KOHEI HAYASHI^{18,19,20}

Draft version December 12, 2017

ABSTRACT

We present wide and deep photometry of the northwest part of the halo of the Andromeda galaxy (M31) using Hyper Suprime-Cam on the Subaru Telescope. The survey covers 9.2 deg² field in the g , i , and $NB515$ bands and shows a clear red giant branch (RGB) of M31's halo stars and a pronounced red clump (RC) feature. The spatial distribution of RC stars shows a prominent stream feature, the North Western (NW) Stream, and a diffuse substructure in the south part of our survey field. We estimate the distances based on the RC method and obtain $(m - M) = 24.63 \pm 0.191(\text{random}) \pm 0.057(\text{systematic})$ and $24.29 \pm 0.211(\text{random}) \pm 0.057(\text{systematic})$ mag for the NW stream and diffuse substructure, respectively, implying that the NW Stream is located behind M31, whereas the diffuse substructure is located in front. We also estimate line-of-sight distances along the NW Stream and find that the south part of the stream is ~ 20 kpc closer to us relative to the north part. The distance to the NW Stream inferred from the isochrone fitting to the color-magnitude diagram favors the RC-based distance, but the TRGB-based distance estimated for $NB515$ -selected RGB stars does not agree with it. The surface number density distribution of RC stars across the NW Stream is found to be approximately Gaussian with a FWHM of ~ 25 arcmin (5.7 kpc), with a slight skew to the south-west side. That along the NW Stream shows a complicated structure including variations in number density and a significant gap in the stream.

Subject headings: galaxies: halos — galaxies: individual (M31) — galaxies: structure

1. INTRODUCTION

Faint stellar halos in disk galaxies like the Milky Way (MW) and Andromeda (M31) serve as fossil records of the formation of such galaxies through hierarchical assembly and past accretion events. In the MW, stars spread over the vast reaches of its halo region are characterized by low metal abundance and high velocity dispersion. The extreme nature of halo stars, compared to stars comprising the disk component, reflects the early dynamical and chemical evolution of the MW, when its appearance differed significantly from what we see today. Extensive analyses of such metal-deficient, old populations have revealed various fundamental properties of the Galactic halo, e.g., the multiple nature in several aspects including its spatial structure, velocity distribution and chemical abundances (e.g., Feltzing & Chiba 2013): the Galactic halo consists of at least two overlapping components: an inner, flattened halo component having high $[\alpha/\text{Fe}]$ ratio, and an outer halo characterized by a more spherical shape, lower metallicity and lower $[\alpha/\text{Fe}]$ ratio. This complicated global structure of the Galactic halo together with recent growing observational evidence for an abundance of stellar streams and other substructures (e.g., Belokurov et al. 2006) suggests that the stellar halo has formed, at least in its outer part, largely from an assembly process of many subsystems, such as dwarf galaxies, as opposed to an in situ dissipative collapse in its inner part. Indeed, this formation picture of stellar halos is suggested by recent numerical simulations of galaxy formation based on standard Λ CDM cosmology (Font et al. 2011). Thus, detailed studies of the halo properties can provide important clues to the understanding of galaxy formation.

M31's halo, the target of this work, is another excellent test-bed for understanding galaxy formation processes through studies of resolved stars in the halo: it provides an external perspective of the nearest large galaxy, where all of M31's stars are about the same distance from us in contrast to the situation in our own Galaxy, which allows us to obtain a relatively complete picture of its stellar halo.

Past observational studies of M31's halo through large photometric and spectroscopic surveys of bright RGB/AGB

¹ Based on data collected at Subaru Telescope, which is operated by the National Astronomical Observatory of Japan

² National Astronomical Observatory of Japan, 2-21-1 Osawa, Mitaka, Tokyo 181-8588, Japan

E-mail: komiya@subaru.naoj.org

³ Graduate University for Advanced Studies (SOKENDAI), 2-21-1 Osawa, Mitaka, Tokyo 181-8588, Japan

⁴ Astronomical Institute, Tohoku University, Aoba-ku, Sendai 980-8578, Japan

⁵ Frontier Research Institute for Interdisciplinary Sciences, Tohoku University, Aoba-ku, Sendai 980-8578, Japan

⁶ Faculty of Pure and Applied Physics, University of Tsukuba, Tennodai 1-1-1, Tsukuba, Ibaraki, 305-8577, Japan

⁷ Current Address: Institute of Management and Information Technologies, Chiba University, 1-33, Yayoi-cho, Inage-ku, Chiba 263-8522, Japan

⁸ Center for Computational Sciences, University of Tsukuba, Tennodai 1-1-1, Tsukuba, Ibaraki, 305-8577, Japan

⁹ CREST, JST, Tennodai 1-1-1, Tsukuba, Ibaraki, 305-8577, Japan

¹⁰ Current Address: Information Technology Center, The University of Tokyo, 5-1-5 Kashiwanoha, Kashiwa, Chiba 277-8589, Japan

¹¹ Department of Astrophysical Sciences, Princeton University, 4 Ivy Lane, Princeton, NJ 08544

¹² UCO/Lick Observatory and Department of Astronomy and Astrophysics, University of California, 1156 High Street, Santa Cruz, CA 95064, USA

¹³ Space Telescope Science Institute, Baltimore, MD 21218, USA

¹⁴ Center for Astrophysical Sciences, Johns Hopkins University, Baltimore, MD, 21218

¹⁵ California Institute of Technology, 1200 E. California Boulevard, MC 249-17, Pasadena, CA 91125, USA

¹⁶ Department of Physics and Astronomy, Seoul National University, Seoul 151-742, Korea

¹⁷ Sydney Institute for Astronomy, School of Physics, University of Sydney, NSW 2006, Australia

stars — e.g., the PAndAS survey using CFHT/MegaCam (McConnachie et al. 2009), the SPLASH survey using KPNO-Mayall/MOSAIC, Keck/DEIMOS and Subaru/Suprime-Cam (Guhathakurta et al. 2005; Gilbert et al. 2006; Tanaka et al. 2010) — have revealed several characteristic properties of M31’s stellar halo, some similar to and some different from those of the MW halo. The similarities to the MW halo are in M31’s outer halo, which has a power-law surface brightness profile, low stellar density and metal-poor stars (Guhathakurta et al. 2005; Kalirai et al. 2006; Gilbert et al. 2012, 2014; Ibata et al. 2014), whereas the differences are seen in the inner halo of M31, which has metal-rich and intermediate-age populations in contrast to largely metal-poor and old halo stars in the MW. The presence of substructures in M31’s halo, such as the Giant Southern Stream, and the non-isotropic distribution of satellites (Ibata et al. 2013), are also seen in the MW.

These observational results for M31’s halo, which provide us a new view of an ancient stellar halo compared to the MW halo, have motivated many subsequent simulations of galaxy formation. Indeed, in Λ -dominated cold dark matter models, each disk galaxy has been developed through a different assembly and evolutionary path: the collapse epoch, star formation history and assembly rate of subsystems are not the same from one halo to another and each stellar halo is thus expected to have a different morphology (e.g., Bullock & Johnston 2005; Cooper et al. 2010). Further observational studies of M31’s halo will thus be of great importance for getting new insights into the formation process of its present structure, especially the origin of the differences relative to the MW halo.

In this work, we report our new observations of M31’s halo using Subaru/Hyper Suprime-Cam (HSC). HSC is a new prime-focus camera on the Subaru Telescope with a 1.5 deg diameter field of view (Miyazaki et al. 2012, 2017; Komiya et al. 2017; Kawanomoto et al. 2017; Furusawa et al. 2017). This combination of HSC and Subaru thus allows us to survey large areas of M31’s halo with only a small number of pointings and to explore much deeper domains of the halo, including faint red giants and horizontal-branch stars, than earlier studies based on 4-m telescopes have revealed. This work will focus on the detailed structure and stellar populations of the northwestern (NW) stream which is full of substructures including dips and gaps, which may have been induced by interaction with orbiting subhalos (Carlberg et al. 2011; Carlberg 2012). Our HSC observations thus provide new insights into the origin of these halo structures.

The paper is organized as follows. In Section 2, we describe our observations of M31’s halo with Subaru/HSC and the method for data analysis. Our target fields are those covering large parts of the NW stream (Figure 1). In Section 3, the spatial distribution of halo stars in our survey regions and their distribution in color-magnitude diagram are presented. Section 4 is devoted to the detailed analysis of stellar populations inside/outside the NW stream, their distance distribution, and the three-dimensional structure of the NW stream. In Section 5, we discuss the nature of the NW stream in comparison to the distribution of globular clusters and a recent numerical simulation of the stream. Finally, we present our conclusions in Section 6.

2. DATA AND METHOD

2.1. Hyper Suprime-Cam Observations

We obtained HSC g - and i -band images during 9 nights in 2014 and 6 nights in 2015. The observing conditions were variable and we devoted observing time in relatively good condition (i.e., fair transparency and better seeing FWHM than $0''.8$) to a deep survey in the halo of M31 which we report on in this paper. Figure 1 shows the target fields, which consist of 5 contiguous pointings (Fields 003, 004, 009, 022 and 023), covering 9.2 deg^2 area in the halo of M31. In each field, dithering with radius of 2 arcmin was performed to cover the gaps between CCDs. During the observation, the transparency was good to fair but the seeing FWHM varied between $0''.45$ and $0''.8$. Total exposure times for each field are 80 min and 80–128 min in the g and i bands, respectively.

We also obtained short exposure images for the 5 target fields using the narrow-band filter $NB515$, which has a bell-shaped transmission curve centered on 515 nm with a band width (FWHM) of 7.7 nm and samples Mgb features of late-type stars (see Figure 2). It is equivalent to the DDO51 filter which is useful to distinguish between giant and dwarf stars based on the depth of stellar surface gravity sensitive spectral absorption features (Morrison et al. 2000; Majewski et al. 2000). Although the $NB515$ exposure times are as short as 16 min for each field, the data are deep enough to separate bright RGB stars of M31 from foreground main sequence (MS) dwarf stars in the MW.

The details of the observations are summarized in Table 1 and the filter response curves are plotted in Figure 2.

2.2. Reduction and Photometry

The HSC data are processed with hscPipe v4.0.1 (Bosch et al. 2017), a branch of the Large Synoptic Survey Telescope pipeline (Ivezic et al. 2008; Juric et al. 2015) calibrated against Pan-STARRS 1 (PS1) photometry and astrometry (Schlafly et al. 2012; Tonry et al. 2012; Magnier et al. 2013). The hscPipe is a standard data reduction pipeline optimized for the data from wide-field mosaic CCD cameras in general and HSC in particular. Each CCD frame is calibrated against PS1 in the course of single frame reduction (i.e., bias subtraction, correction for cross-talk, cosmic ray removal, flat fielding, sky subtraction). Then, all the frames are coadded into a large image based on the mosaicking solution which is calculated using all the frames in each band. Finally, objects are detected and their parameters such as magnitudes, positions, sizes, etc. are measured.

The resultant photometric catalogs in all 3 bands are matched with a matching radius of $0''.5$. In this study, we analyze those objects that are classified as point sources (i.e., *extendedness* = 0 in the hscPipe output catalog) in both g and i bands and PSF magnitudes are used throughout this study except in Section 5.1. Note that the $NB515$ data were calibrated to g -band via hscPipe and the $NB515$ magnitude may be offset systematically from the correct value by ≤ 0.1 mag but the absolute value is not important for our purposes.

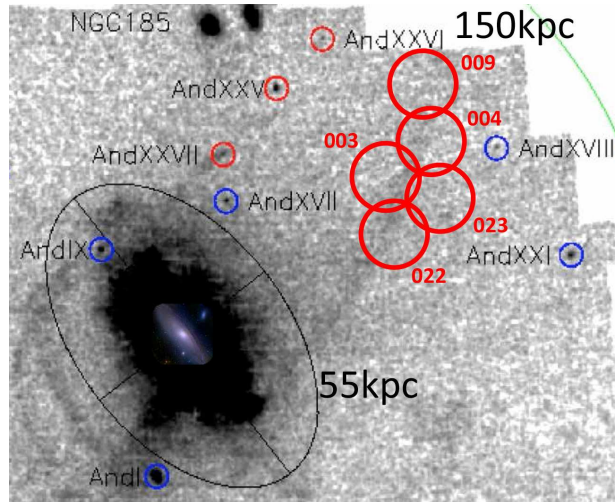


FIG. 1.— The HSC deep survey fields (numbered large red circles) overlaid on Figure 1 of Richardson et al. (2011) showing a central image of M31 and surrounding star count map (grayscale) with some dwarf satellites indicated (small blue and red circles).

TABLE 1
THE DETAILS OF THE OBSERVATION.

| Field | RA, Dec (J2000) | Filter | Exp. Time | Seeing FWHM |
|-------|--|--------------|-----------|-----------------|
| 003 | 00 ^h 16 ^m 31 ^s .7 +44°43′30″ | <i>g</i> | 12×400 s | 0′′.7 – 0′′.8 |
| | | <i>i</i> | 31×240 s | 0′′.5 – 0′′.8 |
| | | <i>NB515</i> | 4×240 s | 0′′.6 – 0′′.75 |
| 004 | 00 ^h 10 ^m 04 ^s .7 +45°27′47″ | <i>g</i> | 12×400 s | 0′′.6 – 0′′.8 |
| | | <i>i</i> | 30×240 s | 0′′.45 – 0′′.8 |
| | | <i>NB515</i> | 4×240 s | 0′′.55 – 0′′.6 |
| 009 | 00 ^h 10 ^m 24 ^s .5 +46°49′07″ | <i>g</i> | 12×400 s | 0′′.65 – 0′′.8 |
| | | <i>i</i> | 20×240 s | 0′′.6 – 0′′.8 |
| | | <i>NB515</i> | 4×240 s | 0′′.55 – 0′′.6 |
| 022 | 00 ^h 16 ^m 04 ^s .2 +43°22′15″ | <i>g</i> | 12×400 s | 0′′.5 – 0′′.8 |
| | | <i>i</i> | 32×240 s | 0′′.45 – 0′′.8 |
| | | <i>NB515</i> | 4×240 s | 0′′.85 – 0′′.95 |
| 023 | 00 ^h 09 ^m 45 ^s .8 +44°06′28″ | <i>g</i> | 12×400 s | 0′′.5 – 0′′.7 |
| | | <i>i</i> | 30×240 s | 0′′.45 – 0′′.7 |
| | | <i>NB515</i> | 4×240 s | 0′′.85 – 0′′.9 |

Our survey is substantially deeper than previous ground-based surveys of M31. We assess how deep our data go by measuring the detection completeness and estimating the extinction by interstellar dust, as described below, before we start further analysis.

The detection completeness is estimated using a PSF model obtained by the hscPipe software for every 4000×4000 pixels grid, which is referred to as a ‘patch’ in hscPipe. A set of 500 artificial stars based on the PSF model and a specific apparent magnitude is embedded in a patch and the hscPipe object detection algorithm is applied. This process is repeated in steps of 0.25 mag and the completeness, the fraction of artificial stars that are detected, is obtained for all the patches. Figure 3 shows the apparent magnitude that corresponds to 50% completeness in *g*, *i* and *NB515* bands over our survey field. The mean magnitudes of 50% completeness in *g*, *i* and *NB515* band are calculated to be 26.31, 25.69 and 24.71 mag, respectively, indicating that our survey is substantially deeper than the previous ground-based studies. Field 023 is the deepest among the survey fields in *g* and *i* bands and the north part is relatively shallow compared to the south part likely due to the unstable weather and variable seeing conditions during the observations. Patches that contain bright stars are shallower than neighboring patches, which indicates that the completeness is degraded by the large halo of a bright star. Therefore, areas occupied by the large halos around bright stars are masked and excluded from the subsequent analysis. The *NB515* band imaging in the north and middle part is deeper than the south part. This is due to variable seeing conditions between the different pointings (see Table 1).

The Galactic extinction is corrected using the new estimate from Schlafly & Finkbeiner (2011) which is based on the dust map by Schlegel et al. (1998). Figure 4 shows the 2 dimensional $E(B - V)$ map for our survey field, where $E(B - V)$ values are taken from NASA/IPAC Infrared Science Archive²¹. The variation of $E(B - V)$ across our survey field is clearly seen in the sense that the northeast part (field 009) suffers from heavy extinction while the majority part of other 4 fields are less affected. Therefore, the extinction correction should be made star by star according to the position on the sky. The mean extinctions in *g*, *i* and *NB515* bands are calculated to be 0.27, 0.14 and 0.24 mag,

²¹ <http://irsa.ipac.caltech.edu/applications/DUST/>

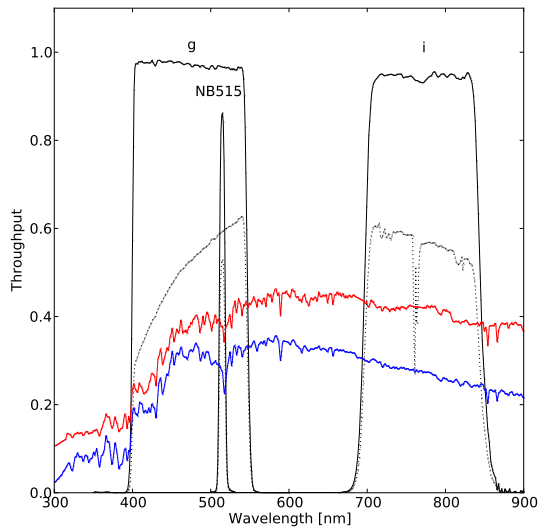


FIG. 2.— Response curves of filters used in the survey. Solid lines show response curves for filters themselves and dotted lines show total response. The spectra of K1V (blue) and K1III (red) stars from Pickles stellar spectral flux library (Pickles 1998) are overlaid. Note that both spectra are averaged for 5 bins (i.e., 2 nm) and the spectrum of K1III star is shifted upwards for clarity.

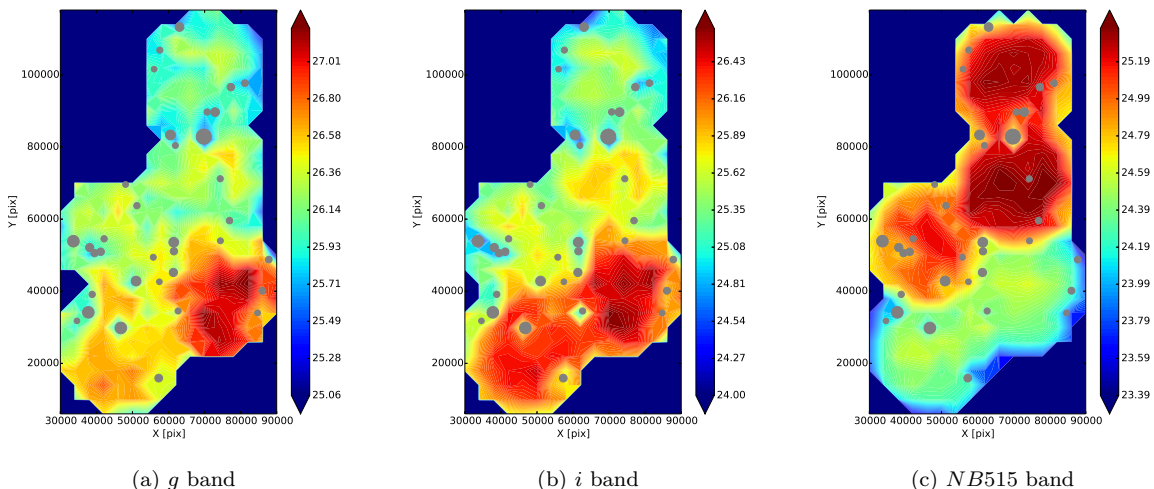


FIG. 3.— The 2 dimensional maps of the 50% completeness magnitude in g (a), i (b) and $NB515$ bands (c). The masked areas by bright stars are shown in gray circles.

respectively. The accuracy in the estimate of extinction based on this method is discussed in Section 4.4.

The spatially varying completeness and extinction resulted in inhomogeneity in the survey depth (i.e., limiting magnitude) across the field, in the sense that the south part (fields 022 and 023) is the deepest and the survey depth gets slightly worse at the middle part (fields 003 and 004) and significantly degraded at the north part (field 009) for g and i bands, while the opposite trend is seen in $NB515$ band. We will take the spatial variation into account in the following analysis. Nonetheless, our data are considerably deep and bring wealth of information to understand the nature of the M31 halo.

2.3. Color-Magnitude Diagram

Figure 5 is the extinction corrected color-magnitude diagram (CMD) of 401,834 catalogued stellar objects down to $i = 27.0$ mag in our survey fields. The photometric error in each band, which is the mean value of every 1 mag bin, is calculated and the errors in the i_0 magnitude and color [calculated for $(g - i)_0 = 1.0$] are plotted as red crosses in the figure. The 50% completeness limit, which is the mean value over the survey field, is plotted as a red dashed line.

The CMD clearly shows the characteristic features: dwarf stars of the MW disk lie on the brightest part of the CMD, extending from $(g - i)_0 \simeq 0.3$ and $i_0 \simeq 19$ to the redder and fainter part of the CMD. A narrow but significant sequence seen at ~ 1 mag fainter from the distribution of the MW disk stars is corresponding to a diffuse stellar stream in the MW halo which is reported by Martin et al. (2014). The RGB in the M31 halo is seen as a broad sequence which

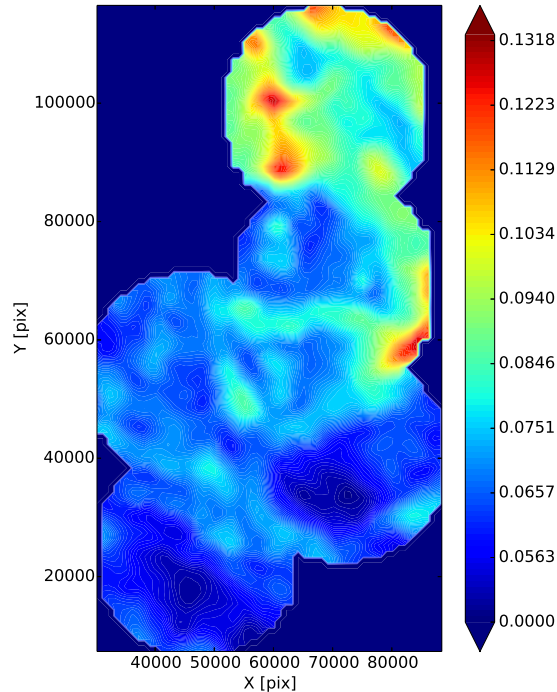


FIG. 4.— The 2 dimensional $E(B - V)$ map for our survey field.

is perpendicular to the above mentioned MW stream and crossing at $(g - i)_0 \simeq 1.1$ and $i_0 \simeq 23$. It is also noted that a significant red clump feature is seen at $(g - i)_0 \simeq 0.8$ and $i_0 \simeq 24.5$ and diffuse but distinct blue horizontal branch (BHB) is also seen at $(g - i)_0 \simeq -0.3$ and $i_0 \simeq 25.5$. We call those object found in $0.3 < (g - i)_0 < 1.0$, $24.0 < i_0 < 25.1$ and $g_0 < 25.6$ as red clump population (RC) in the following analysis. Below $i_0 = 26$, the photometric error becomes large and it is difficult to distinguish characteristic features such as sub-giant branch (SGB) and main-sequence (MS) stars in the M31 halo.

2.4. NB515 and 2-Color Diagram

To extract secure M31's RGB stars behind foreground Galactic dwarf stars, we use a narrow-band filter, *NB515*, in combination with *g* and *i* band filters. This filter has been designed by our team for this purpose and we have already performed a test for distinguishing M31's RGB/AGB stars from foreground Galactic dwarfs using the prototype filter of *NB515* in Suprime-Cam and confirmed its validity. As shown in Figure 2, *NB515* is sensitive to the MgH + Mgb absorption features around 515 nm which is strongly dependent on surface gravity (Majewski et al. 2000, and references therein). By measuring the absorption strength of this feature with *NB515* filter, one can discriminate K giant in the halo of M31 from K dwarfs in the disk of Milky Way with same apparent magnitude. This is illustrated in Figure 2 where the spectra of K1V (blue) and K1III (red) stars from Pickles stellar spectral flux library (Pickles 1998) are well discriminated by the absorption feature, i.e., $NB515 - g$ color in the sense that the $NB515 - g$ color at fixed $g - i$ color is larger for dwarfs and smaller for giants.

We investigate how dwarfs and giants are distributed in the 2-color diagram making use of template spectra in Figure 6 (a). We use Pickles stellar spectral flux library (Pickles 1998) and ATLAS9 stellar atmosphere models (Castelli & Kurucz 2004), and $g - i$ and $NB515 - g$ colors are calculated by convolving the system throughput as shown in Figure 2. Blue, red, green and orange filled circles show normal dwarfs, normal G-K type giants, metal-weak G-K giants and metal-rich G-K giants from Pickles atlas, respectively, and cyan, green and magenta filled triangles with dotted line show dwarfs with solar metallicity, G-K giants with $[Fe/H] = -2.0$ and those with $[Fe/H] = -1.0$ from ATLAS9, respectively. The suggested models²² for dwarfs of ATLAS9 are used for dwarfs with solar metallicity, while T_{eff} and $\log(g)$ are chosen from suggested models for G-K giants and those with different metallicities are used to calculate $g - i$ and $NB515 - g$ colors. The figure indicates that giants can clearly be discriminated from dwarfs for $g - i > 1.0$. Our criteria to select giants, which are represented by the dashed line, fairly well enclose giants except for normal to metal-rich K5 giants.

Figure 6 (b) shows the 2-color diagram for stellar objects with $19 < i_0 < 22$ in our survey field. The thick ' $\sqrt{\quad}$ '-shape sequence is composed of MS dwarf stars of the MW. On the other hand, the giant stars in the M31 halo are populated at around our criteria which are shown as the dashed line. The criteria are set reasonably to select giants in the M31

²² http://www.stsci.edu/hst/observatory/crds/castelli_kurucz_atlas.html

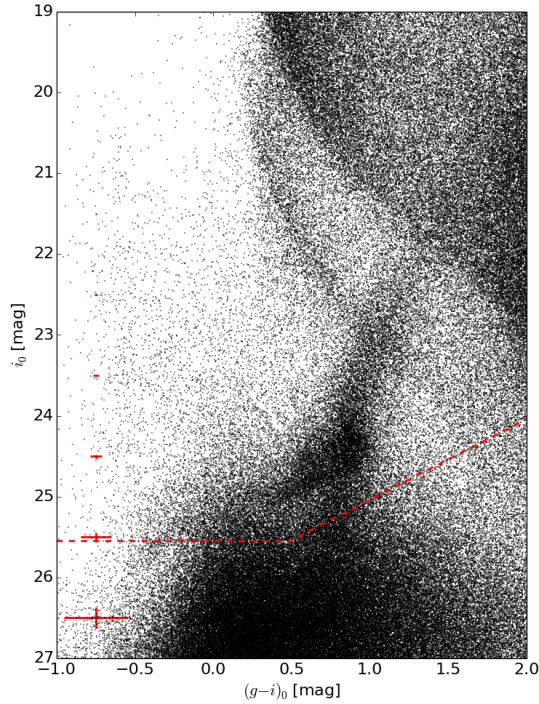


FIG. 5.— Color-magnitude diagram of catalogued stellar objects in our survey field. The photometric error in each band, which is a mean value of every 1 mag bin, is calculated and the errors in the i_0 magnitude and color [calculated for $(g-i)_0 = 1.0$] are plotted as red crosses. The 50% completeness limit, which is the mean value over the survey field, is plotted as a red dashed line.

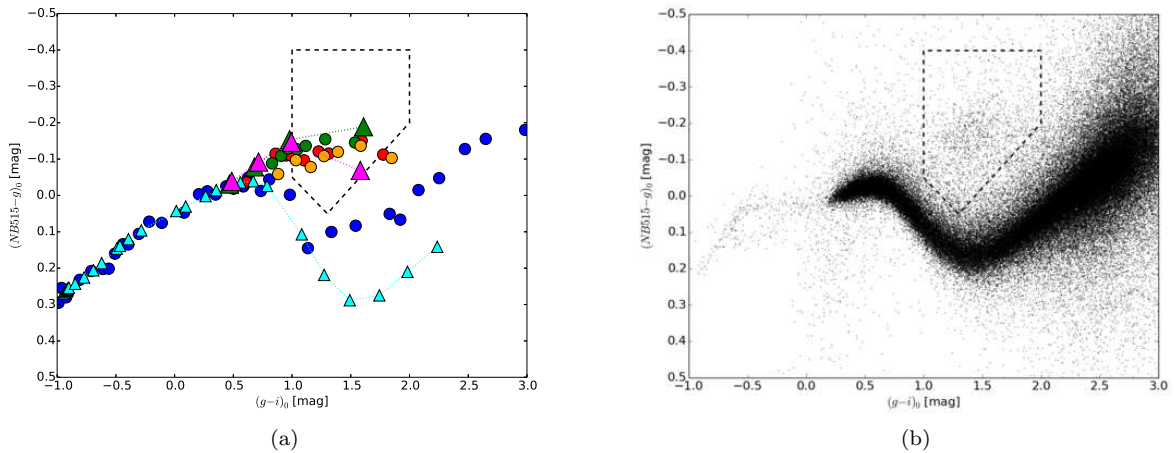


FIG. 6.— (a) $(g-i)$ - $(NB515-g)$ 2-color diagram for template and model stars. Blue, red, green and orange filled circles show normal dwarfs, normal G-K type giants, metal-weak G-K giants and metal-rich G-K giants from Pickles atlas (Pickles 1998), respectively, and cyan, green and magenta filled triangles with dotted line show dwarfs with solar metallicity, G-K giants with $[\text{Fe}/\text{H}] = -2.0$ and those with $[\text{Fe}/\text{H}] = -1.0$ from ATLAS9 (Castelli & Kurucz 2004), respectively. (b) $(g-i)$ - $(NB515-g)$ 2-color diagram for stellar objects with $19 < i_0 < 22$. The stars enclosed in the dashed line are regarded as giant star candidates in the M31 halo (NBGs).

halo while eliminating contaminations from MS dwarfs. In this study, we regard those objects enclosed by the dashed line in Figure 6 to be giant star candidates in the M31 halo and call them as narrow-band selected giants (NBGs).

3. STELLAR POPULATIONS IN THE SURVEY FIELDS

3.1. Spatial Distribution

Figure 7 shows the distributions of NBGs with $19 < i_0 < 23$ and RCs. A distinct stream feature is clearly seen in the figure, which is already shown to exist by the PAndAS survey and called as the NW Stream (McConnachie et al. 2009; Richardson et al. 2011). Our data reveal the much more detailed properties of the NW Stream; The stars consisting of the stream are not uniformly distributed and instead show a clumpy distribution.

Besides the NW Stream, it is pointed out that the surface densities of NBGs and RCs in the off-stream region seem to be higher at the southern part compared to the northern part. This trend may be due to the different limiting magnitude among the survey field, in particular for RC population. We calculate the 50% completeness contour to detect RC population (i.e., those stars with $0.3 < (g - i)_0 < 1.0$, $24.0 < i_0 < 25.1$ and $g_0 < 25.6$), which is plotted as orange dotted line in Figure 7 (b). The figure indicates that most survey field is more than 50% complete, except for the periphery of field of view of HSC pointing at the north part where the extinction is heavy. We therefore conclude that this decreasing trend toward north is real. The same trend is also seen for NBGs, supporting that this trend is real.

In the following, we analyze the data divided into 4 regions, Stream North/South and Off-Stream North/South, and investigate the stellar populations in the 4 regions separately. The boundaries are shown as red dashed lines and each region is labeled in Figure 7. The boundary between north and south ($\delta = 44.8$) is set so that the numbers of stars are almost same between north and south in the off-stream region.

3.2. Color-Magnitude Diagrams of 4 Regions

Figure 8 shows CMDs of 4 regions. In panel (a), overall CMD for each region is plotted with the 50% completeness limit in g and i bands, which is the mean value in each region, and mean error bars for every 1 mag intervals being plotted as a red dashed line and red crosses, respectively, in the respective figure. Panel (b) shows only NBGs and panel (c) shows the zoomed density map of RC regions. The corresponding 50% completeness limit in $NB515$, which is translated from the narrow-band selection criteria, is plotted as a blue dashed line in panel (b). Note that the 50% completeness limit in $NB515$ is only effective for NBGs (red points).

The CMD of the Stream North clearly shows a narrow RGB, populated RC, and a hint of distinct BHB, although the survey depth is shallow, suggesting that the old and metal-poor population is dominated in the Stream North. The peak of RC is found at $(g - i)_0 \simeq 0.6$ and $i_0 \simeq 24.8$ from panel (c).

On the other hand, the CMD of the Stream South shows a different appearance; wider RGB, more abundant RC with multiple peaks, and a tight sequence of BHB. The differences such as the tight BHB sequence may be explained by the difference of the limiting magnitude, but additional stellar populations which are different from that found in the Stream North region is strongly suggested to exist in the Stream South region. Two distinct peaks of RC are found at $(g - i)_0 \simeq 0.6$ and $i_0 \simeq 24.8$ and at $(g - i)_0 \simeq 0.8$ and $i_0 \simeq 24.4$.

The CMD of the Off-Stream South also shows a wider RGB and populated RC, but the morphology of RC is different from those of Stream South/North. In addition, no tight sequence of BHB is observed in the Off-Stream South. The peak of RC is found at $(g - i)_0 \simeq 0.8$ and $i_0 \simeq 24.3$, which seems to be coincide with one of the RC peaks found for the Stream South. This finding indicates that the CMD of the Stream South can be reproduced by a combination of CMDs of the Stream North and the Off-Stream South.

Although the survey depth of the Off-Stream North region is shallow, the CMD of the Off-Stream North is different from that of the Off-Stream South (e.g., populated RC and RGB), suggesting the presence of the diffuse but significant substructure in the Off-Stream South region. It is also noted that the number of NBGs, which are not affected by the survey depth, is smaller compared to that found in each of the other 3 regions [see panels (b)]. These findings lead to the idea that the Off-Stream North region is genuinely the region with no substructure, i.e., part of the smooth halo of M31. The loose RGB sequence and the absence of RC observed for the Off-Stream North also support the idea because stars in the halo are widely distributed along the line of sight direction and the features in the CMD, such as RGB, RC and BHB, are smoothed out along the magnitude axis.

Conclusions of this section are as follows: In addition to the known NW Stream, a diffuse substructure is likely to exist in the south part of our survey field. In the Stream South region, the NW Stream and diffuse substructure overlap. In contrast, the Off-Stream North region seems to be free of substructures and represent a genuine smooth halo of M31. In the following analysis, we regard the Stream North, the Off-Stream South and the Off-Stream North as the representative of the NW Stream, the diffuse substructure and the smooth halo, respectively.

4. BASIC PROPERTIES OF STELLAR POPULATIONS

4.1. Tip of Red Giant Branch (TRGB)

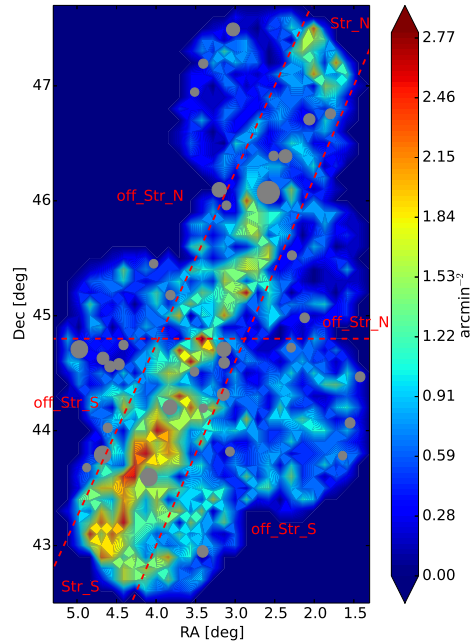
As shown in Figure 5, the bright part of RGB of M31's halo stars is merged into the higher density sequence consisting of numerous MW main sequence stars. We can separate the RGB stars from those overlapping MW main sequence stars by making use of $NB515$ data. TRGB is now visible by plotting NBGs in the CMDs of Figure 8 panels (b).

Following the recent technique to determine the TRGB magnitude based on the Bayesian approach (e.g., Conn et al. 2011; Tollerud et al. 2016; Tanaka et al. 2017), we attempt to determine the TRGB magnitude from NBGs, which are supposed to be a clean sample of RGB in principle, for 4 regions separately. The method we adopt is a maximum-likelihood estimation based on the Markov Chain Monte Carlo (MCMC) algorithm, which is described in detail by Tanaka et al. (2017). In this study, we assume the model luminosity function (LF) as

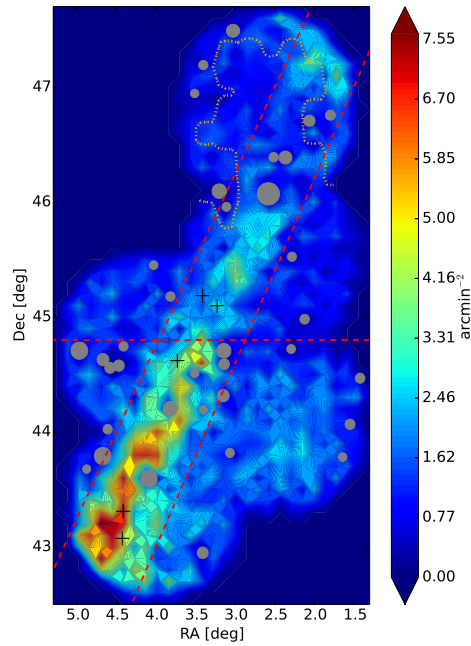
$$\phi(m|m_{TRGB}, a, b) = e^{a(m-m_{TRGB})} + b, \quad (\text{for } m \geq m_{TRGB}) \quad (1)$$

$$= b, \quad (\text{for } m < m_{TRGB}) \quad (2)$$

where m_{TRGB} is the TRGB magnitude. We also assume 100% completeness for our NGB sample. The prior distribution assumed for m_{TRGB} is a normal distribution with the mean, which is estimated from the edge detection algorithm



(a) NBG



(b) RC

FIG. 7.— Surface number density maps of NB-selected RGB stars (a) and RC (b). Areas near bright stars where the object detection is not well carried out are masked as gray circles. The boundaries between Stream/Off-Stream North/South regions are shown in red dashed lines and each region is labeled in the panel (a). In the panel (b), the region where 50 % completeness is achieved at magnitudes of $i_0 = 25.1$ mag and $g_0 = 25.6$ mag, which is the fainter boundary of RC selection, is shown in orange dotted line, indicating that most of the survey field is more than 50 % complete to detect RC stars. Crosses represent 5 globular clusters reported by Huxor et al. (2014) in the survey field.

(Sakai et al. 1996) applied for the data in each region, and $\sigma = 0.5$ mag, and those for a and b are a uniform distribution between 0 and 2. The number of chain used in this study is 4. We also apply a color-cut, $-0.35(i_0 - 23) + 0.7 \leq (g - i)_0 \leq -0.25(i_0 - 23) + 1.5$, to eliminate those stars deviated from RGBs. As shown in panels (b) of Figure 8, this

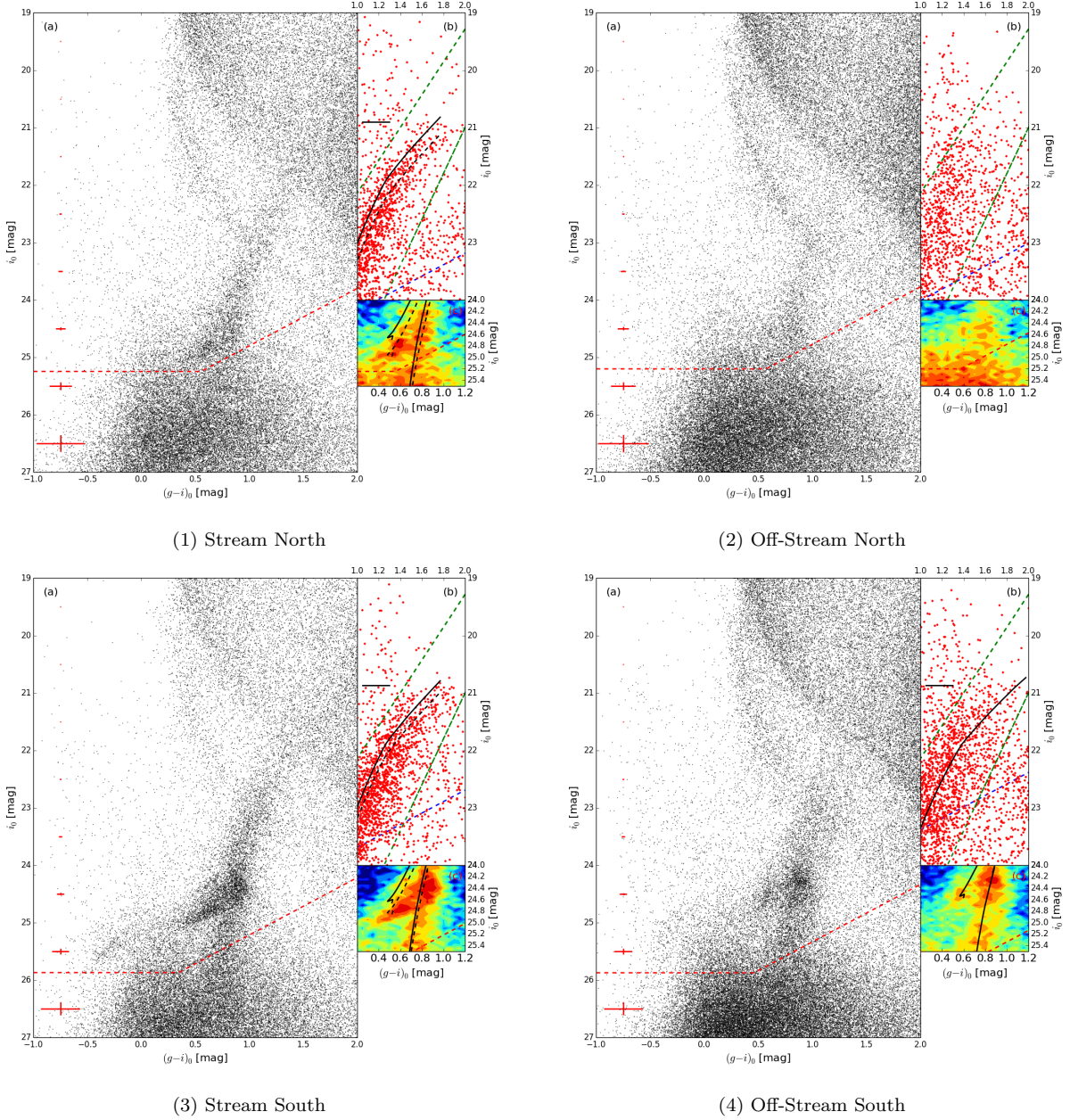


FIG. 8.— CMDs of 4 regions in our survey field. From top-left to bottom-right, CMDs of (1) Stream North, (2) Off-Stream North, (3) Stream South, and (4) Off-Stream South, respectively, are plotted. For each of the parts (1)–(4), panel (a) shows the overall CMD. The 50% completeness limit in g and i bands, which is the mean value in each region, and mean error bars for every 1 mag intervals are plotted as a red dashed line and red crosses, respectively. Panel (b) shows the zoomed view of RGB region with NGBs plotted in red. The corresponding 50% completeness limit in $NB515$ is plotted as a blue dashed line. The RGB selection used to determine the TRGB is plotted as green dashed lines and the TRGB magnitude is indicated in horizontal black bar. The best-fit isochrone is plotted in black thick line. Panel (c) shows the zoomed density map of RC region, together with the best-fit isochrone with the distance modulus determined by TRGB method (back thick line) and that with increasing distance modulus from TRGB by 0.3 (Stream North) and 0.2 (Stream South).

color-cut, which is represented in green dashed lines, clearly excludes outliers and distinguish the TRGB.

Figure 9 shows the result. The blue histogram shows the number distribution of NGBs and the dashed green line shows the frequency of m_{TRGB} obtained from 20,000 MCMC runs after 80,000 unused runs. The orange line is the model LF, $\phi(m_n|m_{TRGB}, a, b)$, for which mean values of m_{TRGB}, a, b are used. The figure clearly shows that the model LF fits the observed distribution of NGBs reasonably well and m_{TRGB} is well determined for Stream North and South regions and fairly determined for Off-Stream South. On the other hand, the determination of m_{TRGB} is poor for Off-Stream North since the number of NGBs found for this region is small and it is difficult to recognize the sharp rise of LF at m_{TRGB} . For comparison, we also plot the edge detection filter described by Sakai et al. (1996) as black dotted lines, suggesting that the both estimates are consistent with each other.

Table 2 summarizes the distribution of m_{TRGB} . We take the peak value as the representative TRGB magnitude

TABLE 2
ESTIMATED TRGB MAGNITUDE FOR 4 REGIONS.

| Region | Mean | Peak | 5% | 25% | 50% | 75% | 95% |
|------------------|-------|-------|-------|-------|-------|-------|-------|
| Stream North | 20.90 | 20.90 | 20.87 | 20.89 | 20.90 | 20.91 | 20.92 |
| Stream South | 20.87 | 20.87 | 20.85 | 20.86 | 20.87 | 20.87 | 20.89 |
| Off-Stream South | 20.79 | 20.84 | 20.58 | 20.78 | 20.83 | 20.85 | 20.86 |

and the 68% interval of the distribution around the peak as the error. We obtain the TRGB magnitudes as $i_0 = 20.90 \pm 0.02$, 20.87 ± 0.02 and 20.84 ± 0.03 mag for the Stream North, Stream South and Off-Stream South, respectively.

The calibration of the absolute magnitude of TRGB is intensively studied by Jang & Lee (2017) and various calibrations are listed in Jang & Lee (2017). For the absolute magnitude of the TRGB, we adopt the calibration by Rizzi et al. (2007):

$$M_{I_c}(\text{TRGB}) = -4.05(\pm 0.02) + 0.22(\pm 0.01)[(V - I_c) - 1.6] \quad (3)$$

When we use the color conversion formula for the relevant range of $1.3 < g - i < 1.7$ (see Appendix A),

$$V - I_c = 0.715(g - i) + 0.317 \quad (4)$$

$$i - I_c = 0.067(g - i) + 0.426, \quad (5)$$

we obtain

$$M_i(\text{TRGB}) = 0.222(g - i) - 3.902 \quad (6)$$

For the TRGB of the Stream North, we find $i_0 = 20.90 \pm 0.033$ and $(g - i)_0 = 1.7$, where the $(g - i)_0$ is the mean color of TRGB, thus equation (6) yields $(m - M) = 24.42$. Similarly, we obtain $(m - M) = 24.39$ and $(m - M) = 24.31$ for those of the Stream South and Off-Stream South.

The error of $(m - M)$ is calculated as follows: For the random error, we take the errors from Rizzi equation (Eq. 3), the error from the TRGB determination ($\sigma = 0.02$), and the width of the TRGB color ($\sigma = 0.1$) and then calculate the root square sum of all the propagated errors. For the systematic error, we take the errors from the fitting of color conversions ($\Delta = 0.017$ and $\Delta = 0.009$ for Eqs. 4 and 5) and the absolute photometric calibration ($\Delta = 0.02$) and then calculate the sum of all the propagated errors. The random and systematic errors are calculated to be 0.033 and 0.033, respectively, for the Stream North and South and those for the Off-Stream South are 0.040 and 0.033. The distances derived from TRGBs and their errors are summarized in Table 3.

4.2. Stellar Population of RGB, RC, and RGB bump

To determine the absolute luminosities of specific features in a CMD, such as RC and RGB bump (RGBb), we need to set the age, τ_{age} , and metallicity, Z , of stellar population in both stream and off-stream regions. For this purpose, we attempt to reproduce both the locus of RGB and the relative position of RC in a CMD for the ranges of τ_{age} and Z , based on a Padova isochrone with a fiducial value for mass-loss parameter on RGB of $\eta = 0.2 - 0.5$. The color system of the isochrone (SDSS system) is converted to the HSC system as described in Appendix A.

First, we adopt the distance modulus determined by TRGB method described in Section 4.1 and look for the best-fit isochrone. For the Off-Stream South, we find that the isochrone with $Z = 0.0014$ ($[\text{Fe}/\text{H}] = -1.13$), $\log \tau_{\text{age}}(\text{Gyr}) = 10.00$ and $\eta = 0.3$ traces the RGB and RC features perfectly [see Figure 8 (4)-(b) and (4)-(c)]. On the other hand, it is found to be difficult to fit the isochrones to the CMDs of Stream North and Stream South, in particular, to the RC features [see black thick lines in Figure 8 (1)-(c) and (3)-(c)]. We therefore try to fit the isochrone by changing the distance modulus and find that the isochrone with $Z = 0.0008$ ($[\text{Fe}/\text{H}] = -1.37$), $\log \tau_{\text{age}}(\text{Gyr}) = 10.00$ and $\eta = 0.3$ traces the RGB and RC features for Stream North and Stream South by increasing the distance modulus by 0.3 and 0.2 mag, respectively [see black dashed lines in Figure 8 (1)-(c) and (3)-(c)]. We note that the ‘deep dip’ in LF is found for the Stream North at $i_0 \simeq 21.14$ mag, which is in contrast to the monotonic increase of RGB population toward fainter magnitude found for most galaxies. This may suggest that the real RGB population in the Stream North emerges from $i_0 \sim 21.14$ mag. The edge detection filter suggests the peak at $i_0 \simeq 21.22$ which is consistent with the suggestion from isochrone fitting. Note the typical metallicity range estimated from the width of RGB is $\sigma_{[\text{Fe}/\text{H}]} \sim 0.2$, which is used in what follows.

4.2.1. Red Clump

Figure 10 shows the zoomed view of the CMDs in the form of density map around RC where we note that the vertical axis is now g -band magnitude in this figure. Significant peaks of RC at $(g - i)_0 \simeq 0.6$ are found in the CMDs for the Stream North, Stream South and the Off-Stream South. It is also suggested that the CMD around RC for the Stream South can be reproduced by the combination of the CMDs for the Stream North and the Off-Stream South. No significant peak is found for the Off-Stream North but this is naturally understood if the Off-Stream North region is a representative of a smooth halo (see Section 3.2).

We measure the color and magnitude of the peak of RC for each region. They are measured to be $(g - i)_0 = 0.562 \pm 0.085$ and $g_0 = 25.456 \pm 0.132$ for the Stream North and $(g - i)_0 = 0.568 \pm 0.080$ and $g_0 = 25.122 \pm 0.160$ for the Off-Stream South. Here, we adopt the standard deviation around the peak of RC as errors. Since two different

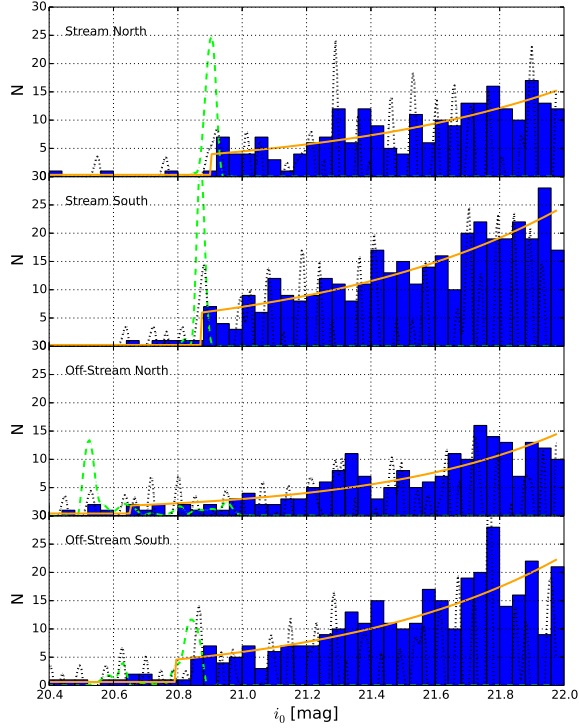


FIG. 9.— The blue histogram shows the number distribution of NBGs and the dashed green line shows the frequency of m_{TRGB} obtained by 20,000 MCMC runs after 80,000 unused runs. The orange line is the model LF, $\phi(m_n|m_{TRGB}, a, b)$, for which mean values of m_{TRGB}, a, b are used. For comparison, we also plot the edge detection filter described by Sakai et al. (1996) as black dotted lines.

structures are suggested to be overlapping in the Stream South region and no significant peak is found for the Off-Stream North, we do not attempt to derive the color and magnitude of RC for these two regions.

For the absolute magnitude of RC, we adopt the calibration by Bilir et al. (2013):

$$M_V(\text{RC}) = 0.627(\pm 0.104)(B - V)_0 + 0.046(\pm 0.043)[Fe/H] + 0.262(\pm 0.111). \quad (7)$$

When we use the color conversion formula for the relevant range of $0.4 < g - i < 1.2$ (see Appendix A),

$$g - V = 0.371(g - i) + 0.068 \quad (8)$$

$$B - V = 0.709(g - i) + 0.170, \quad (9)$$

we obtain

$$M_g(\text{RC}) = 0.8155(g - i) + 0.046[Fe/H] + 0.4366 \quad (10)$$

Using eq. (10) combined with the metallicity of $[Fe/H] = -1.38$ (see Section 4.2), we obtain $M_g(\text{RC}) = 0.831$ and thus $(m - M) = 24.63$ for the RC of the Stream North. For the RC of the Off-Stream South, we obtain $M_g(\text{RC}) = 0.848$ and thus $(m - M) = 24.27$.

The error of $(m - M)$ is calculated in the similar way to the calculation for TRGB. For the random error, we take the errors from Bilir equation (Eq. 7), the error of the RC magnitude, the error of the RC color, and the error of the metallicity ($\sigma = 0.2$) and then calculate the root square sum of all the propagated errors. For the systematic error, we take the errors from the fitting of color conversions ($\Delta = 0.029$ and $\Delta = 0.019$ for Eqs. 8 and 9) and the absolute photometric calibration ($\Delta = 0.02$) and then calculate the sum of all the propagated errors. The random and systematic errors are calculated to be $0.191 \sim 0.211$ and 0.057 , respectively. The distances derived from RC and their errors are summarized in Table 3.

4.2.2. RGB Bump

In Figure 10, RGBb features are recognized at $(g - i)_0 \simeq 0.8$ for the Stream North, Stream South and Off-Stream South. This feature is most prominent at the Off-Stream South, suggesting that this feature at $(g - i)_0 \simeq 0.8$ and $g_0 \simeq 25.2$ is characteristic for the Off-Stream South, i.e., the diffuse substructure. Looking at the CMD of the Stream South, a peak is found at the same position as the Stream South, and the other peak is found at $(g - i)_0 \simeq 0.8$ and $g_0 \simeq 25.4$, which is suggested to be the bump feature of the M31 NW Stream and should also be found at the Stream North. Bearing this in mind, we measure the color and magnitude of RGBb feature for the Stream North and

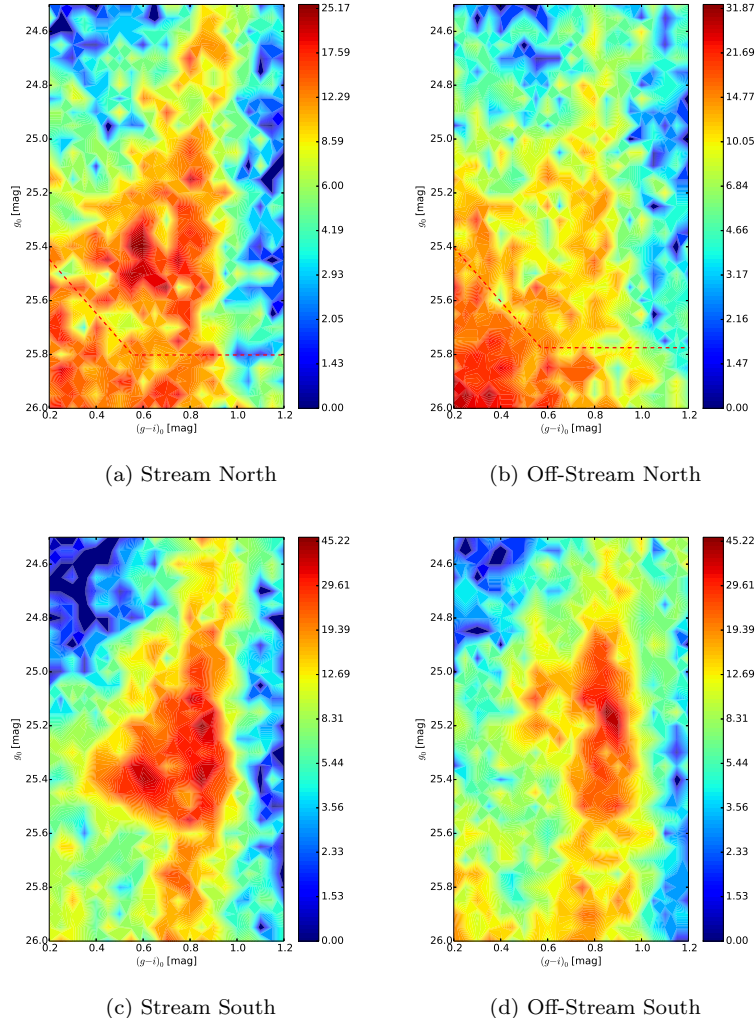


FIG. 10.— Zoomed CMDs in the form of density map around RC of 4 regions in our survey field. From top-left to bottom-right, CMDs of (a) Stream North, (b) Off-Stream North, (c) Stream South, and (d) Off-Stream South, respectively, are plotted. The grid widths used in these figures are $\Delta(g-i) = 0.05$ and $\Delta g = 0.05$ mag. Note that the vertical axis is g -band magnitude.

Off-Stream South regions. They are measured to be $(g-i)_0 = 0.830 \pm 0.076$ and $g_0 = 25.478 \pm 0.097$ for the Stream North and $(g-i)_0 = 0.857 \pm 0.076$ and $g_0 = 25.112 \pm 0.110$ for the Off-Stream South.

Alvez & Sarajedini (1999) show the table on the V -band absolute magnitude of RGBb, $M_V(\text{RGBb})$, for stellar population with different age and metallicity. The interpolation of the table gives $M_V(\text{RGBb}) = 0.177$ and $M_V(\text{RGBb}) = 0.477$ for the Stream North and Off-Stream South, respectively. Thus, using eq. (8) to estimate V -band magnitude from the values of g_0 and $(g-i)_0$ of RGBb, we obtain the distance modulus $(m-M)$ to each region. For RGBb of the Stream North, our estimate of $(g-i)_0 = 0.830$ and $g_0 = 25.478$ yields $V = 25.102$, then $(m-M) = 24.93$. For RGBb of the Off-Stream South, our estimate of $(g-i)_0 = 0.857$ and $g_0 = 25.112$ yields $V = 24.726$, then $(m-M) = 24.25$. The derived distance moduli are consistent with the tendency obtained from RC methods that the Stream North (the NW Stream) is located at farther than the Off-Stream South (the diffuse substructure). Note that Alvez & Sarajedini (1999) relation seems to be very sensitive to the metallicity and age of the population and the present estimate would have large uncertainty.

4.3. Summary of Distance Estimates of Stellar Populations

Table 3 summarizes the distance moduli measured by different methods presented here. The Off-Stream South region shows small variation in the distance moduli estimated from different methods. However, the difference between the distance modulus derived from TRGB and that from RC is large for the Stream North region. This difference is relaxed if the distance modulus from TRGB is increased by 0.2-0.3 mag, which is suggested from the isochrone fitting (see Section 4.2). We therefore prefer to use the distance moduli derived from RC method for the following analysis.

Considering that the distance modulus of M31 is 24.45 mag (776 kpc), which is the median of 345 measurements compiled by NASA/IPAC Extragalactic Database (NED)²³, the NW Stream of our survey field is located behind

²³ <http://ned.ipac.caltech.edu/>

TABLE 3
THE SUMMARY OF DISTANCES CALCULATED IN THIS STUDY.

| Field | Stream North | Stream South | Off-Stream South |
|--------------------|--------------|--------------|------------------|
| (m-M) from TRGB | 24.42 | 24.39 | 24.36 |
| (random error) | ± 0.033 | ± 0.033 | ± 0.040 |
| (systematic error) | ± 0.033 | ± 0.033 | ± 0.033 |
| (m-M) from RC | 24.63 | - | 24.29 |
| (random error) | ± 0.191 | - | ± 0.211 |
| (systematic error) | ± 0.057 | - | ± 0.057 |
| (m-M) from RGBb | 24.77 | - | 24.39 |

TABLE 4
THE SUMMARY OF DISTANCES OF NW STREAM.

| Field | Center Coordinates [deg] | (m-M) | (m-M) Error (random/systematic) | Distance [kpc] |
|----------|--------------------------|-------|---------------------------------|----------------|
| Stream 1 | (2.06, 46.90) | 24.64 | $\pm 0.196 \pm 0.057$ | 847 |
| Stream 2 | (3.00, 45.45) | 24.62 | $\pm 0.186 \pm 0.057$ | 839 |
| Stream 3 | (3.78, 44.25) | 24.59 | $\pm 0.183 \pm 0.057$ | 828 |
| Stream 4 | (4.52, 43.10) | 24.58 | $\pm 0.185 \pm 0.057$ | 824 |

M31 by ~ 90 kpc if we adopt the distance modulus derived from RC for the Stream North. In contrast, the diffuse substructure, which is represented by the Off-Stream South found by this study is located at more than ~ 30 kpc in front of M31.

4.4. 3D Structure of the M31 NW Stream

To understand the nature of the M31 NW Stream, it is important to obtain the distance information for the M31 NW Stream. If the 3D structure of the NW Stream is obtained, then this information gives a useful constraint on the origin of the stream.

In this section, we investigate the distances to the NW Stream by dividing the stream regions (i.e., Stream North and South) into 4 regions. The boundaries are set as $\delta = 43.7, 44.8$ and 46.1 and we name the regions Stream 1 to 4 from the north to south. Due to the issues on the TRGB distances discussed in the previous Section, we adopt the RC method as described in Section 4.2.1 to address the distance distribution along the NW stream.

Figure 11 shows the background/foreground-subtracted CMDs (HESS diagrams) around RC. The CMD of the background/foreground objects for the Stream 1 region is made from those stars which reside outside the stream region with the same declination range as the Stream 1 region (i.e., $\delta > 46.1$). The CMDs of the background/foreground objects for the Stream 2-4 regions are made in the same way. In each panel, individual stars in the stream regions are also plotted as black dots, aiming to show the real distribution of stars in each CMD. We measure the mean color and magnitude of the RC for each region and find $(g-i)_0 = 0.562 \pm 0.085$ and $g_0 = 25.467 \pm 0.139$, $(g-i)_0 = 0.562 \pm 0.084$ and $g_0 = 25.447 \pm 0.125$, $(g-i)_0 = 0.569 \pm 0.085$ and $g_0 = 25.430 \pm 0.119$, and $(g-i)_0 = 0.573 \pm 0.083$ and $g_0 = 25.420 \pm 0.123$ for the Stream 1 to 4 regions, respectively. The distance moduli derived from the RC method are 24.64, 24.62, 24.59, 24.58 for the Stream 1 to 4, respectively (see Table 4). Note that the Stream 1 is shallow in terms of the completeness but the peak of the RC seems to be reasonably measured since it is found at ~ 0.2 mag brighter than the 50% completeness limit.

As explained in Section 2.2, the Galactic extinction is corrected for every single star using the new estimate from Schlafly & Finkbeiner (2011) which is based on the dust map by Schlegel et al. (1998). The reddening $E(B-V)$ ranges from ~ 0 to 0.1318 within our survey field (see Figure 4) which corresponds to the maximum extinction of $A_g = 0.4858, A_i = 0.2440$. Therefore, the error in the reddening map would introduce additional error for extinction-corrected magnitudes. It is noted that the variation in extinction-corrected color $(g-i)_0$ of the RC along the stream is as small as 0.01 mag. This suggests that our method to correct extinction is carried out properly given that the stellar population is homogeneous along the stream.

Although the uncertainty in the RC method is large, the result indicates that the south part of the NW Stream is ~ 20 kpc closer to us (and M31) relative to the north part (see the right panel of Figure 16). The angle between the Stream 1 and 4 is ~ 4.2 deg, which corresponds to the projected distance of ~ 61 kpc, indicating that this configuration seems to be realistic. The angle from the Stream 4 to the major axis of M31 along the stream is roughly 6 deg (see Figure 1), which corresponds to the projected distance of ~ 90 kpc. The line of sight distance between Stream 4 and M31 is calculated to be ~ 50 kpc. If the NW Stream is extended to the south-east direction with the same rate as that found in our survey field, it is still behind M31 when it crosses the major axis of M31. Therefore, we conclude that the NW Stream is a part of an orbiting stream around M31 on the farther side of M31.

4.5. Shape of the M31 NW Stream

Figure 12 shows the number density distributions of RC stars for the Stream 1 to 4 field along the direction perpendicular to the NW Stream, where the coordinate X_r increases towards the south-west direction as clarified in

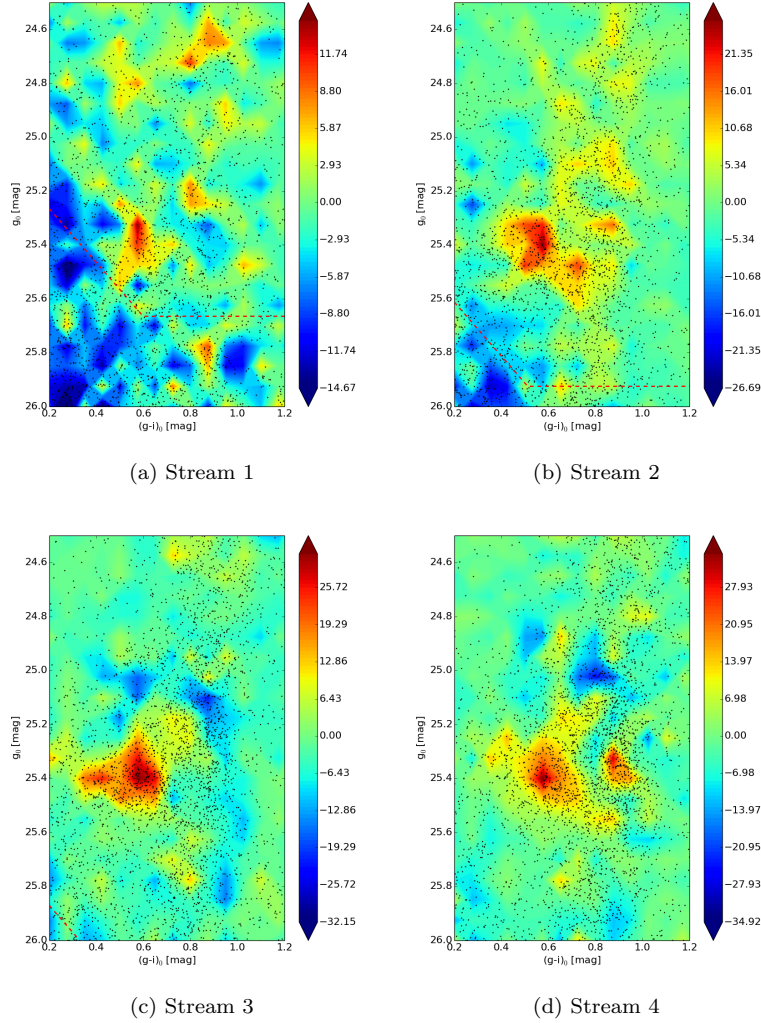


FIG. 11.— Background/foreground-subtracted CMDs (HESS diagram) around RC of 4 regions along the NW Stream. From top-left to bottom-right, CMDs of (a) Stream 1, (b) Stream 2, (c) Stream 3 and (d) Stream 4, respectively, are plotted. In each panel, individual stars in the stream region are also plotted as black dots. The grid widths used in these figures are $\Delta(g-i) = 0.075$ and $\Delta g = 0.075$ mag.

the top panel of Figure 13. Although our survey does not fully cover the south-west side (i.e., $X_r > 18$) of the Stream 1 field and the north-east side (i.e., $X_r < -30 \sim -24$) of the Stream 2-4 field, figures for Stream 2 and 3 clearly show the number density distribution across the NW Stream.

The overall shape can be fitted by the combination of a Gaussian with FWHM of ~ 25 arcmin and a linear function for the Stream 2 and 3 fields. It is noted that the distribution seems to be slightly skewed: the south-west side of the stream (i.e., right side of the distribution in the figures) shows steep rise ($\sim 0.06 / \text{arcmin}^3$ for $6 < X_r < 18$) while the north-east side shows rather shallow rise ($\sim 0.03 / \text{arcmin}^3$ for $-18 < X_r < -6$) in the Stream 3 field. Similar trend is also seen for the Stream 2 and 4 fields. This may tell something on the formation process of the NW Stream. The Stream 1 field shows no prominent peak at around $X_r = 0$, but a hint of overdensity is clearly visible from Figure 7. The overdensity seems to be extended to north-west beyond our survey fields, thereby further observation to this direction is required to investigate the detailed shape for the Stream 1 field.

The middle panel of Figure 13 (a) shows the number density distributions of RC stars along the NW Stream, where the coordinate Y_r increases towards the north-west direction. The blue histogram represents the surface number density of RC stars within a width of 44.8 arcmin centered on the stream. The width of 44.8 arcmin corresponds roughly to $\pm 2\sigma$ of the Gaussian fitted for Stream 2 and 3. The positive Y_r corresponds to the north-west side of the NW Stream as clarified in the top panel of Figure 13 (a). The green and red histograms represent those for outside the stream on the north and south side, respectively. The histograms are calculated using those RC stars found in 1.5σ width regions, although our survey does not always cover these regions. Therefore, the red and green histograms should be taken as a guide to estimate the foreground/background contamination to the surface number density of RC stars of the NW Stream.

The blue histogram outnumbers the green and red histograms for the most part of the figure, indicating that the stream is found for all through our survey field. It is also noted that the surface number density varies dramatically along

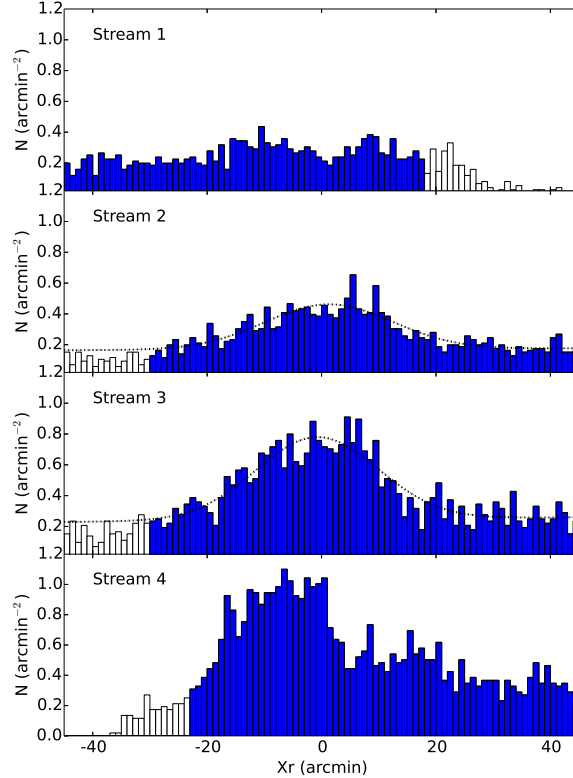


FIG. 12.— The number density distributions of RC stars along the direction perpendicular to the NW Stream. From top to bottom, the histograms for the Stream 1 to 4 are shown. The positive X_r corresponds to the south-west side of the NW Stream. The areas shown in white histograms are where our survey coverage is incomplete. The best-fit profile, which is a combination of a Gaussian and a linear function, is plotted as a dotted line in the Stream 2 and 3 fields.

the stream and several gaps are found in the stream. We try to estimate the foreground/background subtracted number density distribution of RC stars assuming that the maximum of the green and red histograms at fixed Y_r represents the foreground/background. The bottom panel of Figure 13 (a) shows the foreground/background subtracted number density distributions in each bin (dotted line) and a moving average over 5 bins (thick line). The surface number density is the highest at $Y_r = 13$ arcmin and is 0.66 ± 0.10 arcmin $^{-2}$ (Poisson error is assumed). The overall surface number density gradually decreases as Y_r increases, with bumps and dips along the stream. Since the typical error ranges from 0.05 to 0.1 arcmin $^{-2}$, most of bumps are statistically significant. The most significant gap is found at $210 < Y_r < 240$, which is also clearly seen in Figure 7. It is again recovered at $Y_r > 240$ though the surface number density is the lowest among our survey field. However, the significance of this rise is uncertain since the lower completeness than 50% for $Y_r > 240$ is suggested from Figure 7 (b). Comparing the top and bottom panels of Figure 13 (a), the peak positions are not coincident with the globular clusters found on the NW Stream (Huxor et al. 2014).

We also made a similar figure for NBGs as shown in Figure 13 (b). Since the error in surface number density is calculated to be between 0.02 and 0.05 arcmin $^{-2}$ (Poisson error is assumed), the significance of the features seen in the bottom panel of Figure 13 (b) is low compared to that of Figure 13 (a). But it is suggested that the overall shape along the stream, such as the gap at $210 < Y_r < 240$, the bump at $150 < Y_r < 200$, and the gradual increase in the number density distribution toward smaller Y_r , is similar between RCs and NBGs except for $Y_r < 30$, where the derived number density seems to be affected by a clump of NBGs found at $(X_r, Y_r) = (30, 15)$. Unfortunately, the fine structures such as the numbers of sharp peaks seen in the bottom panel of Figure 13 (a) are not confirmed by NBGs due to the shortage of statistical significance.

Recently, many studies on the formation of gaps in the stellar streams due to the encounter of Λ CDM substructures have been carried out (e.g., Carlberg et al. 2011; Carlberg 2012; Erkal et al. 2016). Our data provides an excellent observational example to test these simulations. It is also noted that the bumps found in the bottom panel of Figure 13 (a) seems to be periodic, which is reminiscent of the epicyclic bumps seen in simulations of star clusters (e.g., Kupper et al. 2012).

Carlberg (2012) investigated the density profile of the NW Stream using PAndAS data (Carlberg et al. 2011). They showed the density profile with a moving average over 5 or 11 bins of $0^\circ.25$. This indicates that the resolution of their analysis is $> 0^\circ.25$, an order lower than ours. Therefore, our data are complementary to theirs and would be of help to understand the detail of the density profile at the small scale.

5. DISCUSSION

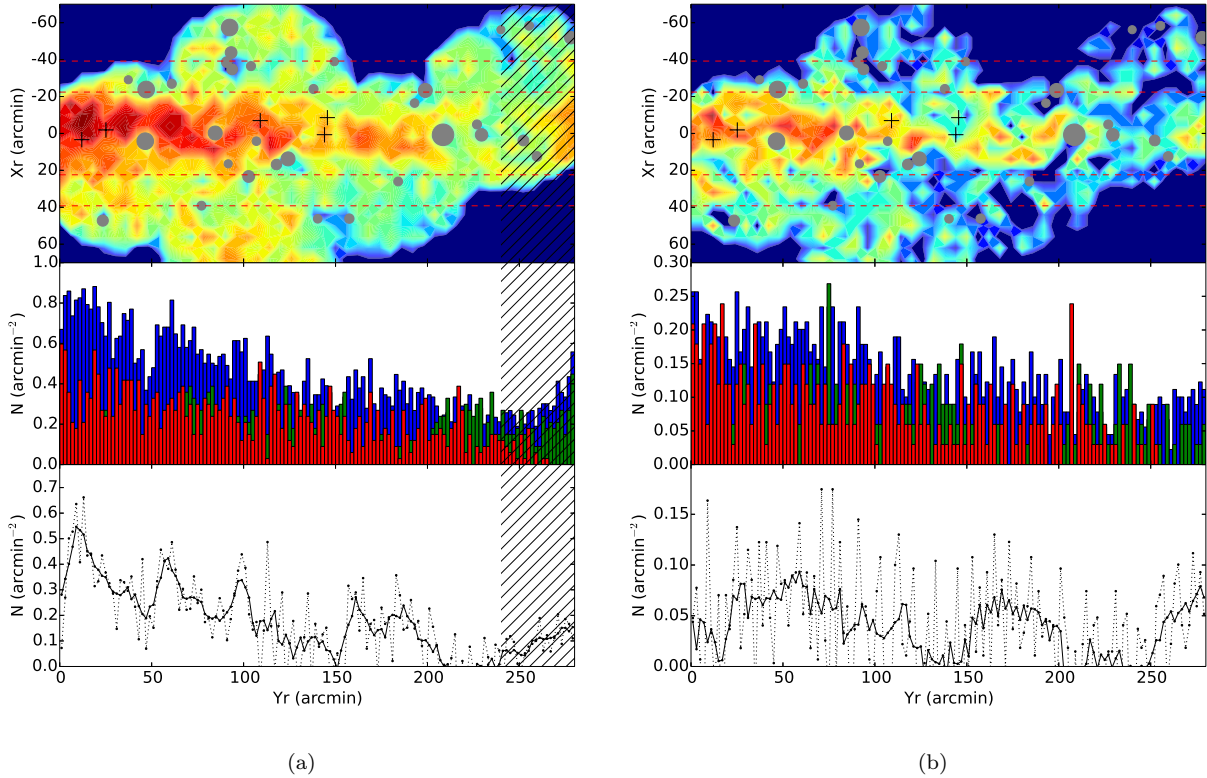


FIG. 13.— (a) The shape of the NW stream represented by RCs: (Top) The spatial distribution of RC stars on the Xr-Yr coordinates system. The red dashed lines indicate the division lines between blue/green/red histograms, i.e., $\pm 2\sigma$ and $\pm 3.5\sigma$ of the Gaussian fitted for Stream 2 and 3. The crosses represent the positions of globular clusters found on the NW Stream by Huxor et al. (2014). (Middle) The number histograms of RC stars along the direction of the NW Stream. The blue histogram represents the surface number density of RC stars within the width of 44.8 arcmin (i.e., $\pm 2\sigma$). The green and red histograms represent the surface number density of RC stars outside the above region to the north and south, respectively. The positive Yr corresponds to the north-west side of the NW Stream. (Bottom) The best-estimated foreground/background subtracted surface number density distribution of RC stars along the direction of the NW Stream. The foreground/background is estimated assuming that the maximum of the green and red histograms of middle figure at fixed Yr and is subtracted from the blue histogram. The dotted line represents the subtracted number density and the thick line represents the moving average over 5 bin (i.e., 10 arcmin). Note that the Yr>240 region where lower completeness than 50% is suggested from Figure 7 (b) is hatched in the figure. (b) Same figure as (a), but for NBGs.

5.1. Properties of Globular Clusters on the NW Stream

Huxor et al. (2014) reported their discovery of 59 globular clusters (GCs) and 2 candidates in the halo of M31 based on the PAndAS survey data. Follow-up spectroscopic observations carried out by Veljanoski et al. (2014) obtained the radial velocities for 78 GCs. Now the large sample of GCs are available and the detailed studies of GCs can be possible even for M31.

Among these GCs, 7 GCs show a hint of association with the NW Stream and 5 share a clear trend in corrected radial velocity as a function of projected radius (Veljanoski et al. 2014), suggesting the same origin as the NW Stream. Our survey field contains 5 GCs and they are found to be located near the center of the stream, suggesting their association with the stream (Figure 7). Out of 5 GCs, 3 GCs located at the south of our survey field (PAndAS-11 to 13) clearly trace the high surface number density regions as shown in Figure 7. On the other hand, the rest 2 (PAndAS-9 and 10) are located at relatively low surface number density region (Yr=140 in Figure 13).

Making use of our high image quality data, we carry out a detailed study for these GCs in combination with the NW Stream to investigate the relation between these GCs and the NW Stream. Unfortunately, 1 GC (PAndAS-9) is buried in the halo of a bright star ($V=10$), making it difficult to detect stars belonging to the GC. We carried out the detailed analysis for the rest 4 GCs, PAndAS-10 to 13. DAOPHOT PSF photometry software (Stetson 1987, 1994) is applied for these GCs and CMDs based on DAOPHOT photometry are plotted in Figure 14. Those stars with good fitting quality ($Sharpness < 1$) are plotted as large dots and others are as small dots. The mean photometric errors are calculated for every 1 mag range and plotted as crosses at $(g-i)_0 = -0.25$. All the CMDs show clear sequences of RGB stars although the scatters are slightly larger than that observed for Stream North [Figure 8 (a)]. In each CMD, an isochrone of RGB which best traces the distribution of RGB stars $[(\log \tau_{\text{age}}, Z) = (10.12, 0.002), (10.00, 0.001), (10.00, 0.002) \text{ and } (10.12, 0.001) \text{ for PAndAS-10 to 13, respectively, with } (m-M)=24.63]$ is plotted for guide.

Comparing these CMDs with that for the Stream North, no significant difference in the position of RGB in the CMD is seen between the Stream North and all the GCs, indicating that the stellar populations consisting of GCs are similar to that of the stream. It is also noted that the brightest RGB star in each GC is equal to or fainter than

the tip of the isochrone, which is consistent with the condition that GCs are located near or farther than the distance of $(m-M)=24.63$, except for PAndAS-13 in which a star with $i_0 = 20.4$ is found. Note that Veljanoski et al. (2014) pointed out that PAndAS-13 is displaced from the linear relation in radial velocity with the projected radius observed for other 5 GCs (PAndAS-4, 9 to 12). The results support the idea that both GCs (PAndAS 10-12) and the stream are originated from same progenitor system and share a same orbit in the halo of M31.

It is also pointed out that small difference in stellar population of GCs is suggested from isochrone fitting. This difference is supported by the integrated photometry for these GCs by Huxor et al. (2014) which shows that PAndAS-10 and 12 are redder [$(g-i)_0 = 0.75$ and 0.75 , respectively] than PAndAS-11 and 13 [$(g-i)_0 = 0.67$ and 0.65 , respectively]. Therefore, the small difference in stellar population of GCs seems to be real. Follow-up spectroscopic observations to measure the metallicity would give an answer for the stellar population of these GCs.

5.2. Comparison with Simulation

Kirihara et al. (2017b) recently carried out an extensive numerical simulation to constrain the orbits and physical properties of the progenitor of the NW Stream, provided that 5 GCs on the NW Stream (PAndAS-04, 09, 10, 11 and 12) share the same orbit as the NW Stream, thereby making use of the radial velocities of these GCs. They showed that the allowable orbits of the NW Stream are divided into two branches: one that the stream is located in front of M31 with line-of-sight distances of apocenter D_{apo} of 430~680 kpc, and the other that the stream is located behind M31 with D_{apo} of 880~1100 kpc (see also Figure 15 b).

The key to constrain the orbit is the line-of-sight distance to the NW Stream, which we derived as 824-847 kpc from RC method (see Table 4). Combined with our distance measurement, we carried out test-particle simulations. A test-particle is launched from the position of the GC PAndAS-12 in the gravitational potential of M31. The potential consists of a Hernquist bulge (Hernquist 1990), an exponential disk and an NFW dark matter halo (Navarro et al. 1996) following Kirihara et al. (2017a). The M31 bulge is set to have the scale radius of 0.61 kpc and the total mass of $3.24 \times 10^{10} M_{\odot}$. The scale height, radial scale length, total mass and central surface density of the M31 disk are 0.6 kpc, 5.4 kpc, $3.66 \times 10^{10} M_{\odot}$ and $2.0 \times 10^8 M_{\odot} \text{ kpc}^{-2}$, respectively. The inclination and position angle of M31's disk are 77° and 37° , respectively (Geehan et al. 2006). The scale radius and scale density of the NFW halo are 7.63 kpc and $6.17 \times 10^7 M_{\odot} \text{ kpc}^{-3}$, respectively. The radial velocity of the test-particle is set to 472 km s^{-1} , which is the observed value of PAndAS-12 (Veljanoski et al. 2014). Its initial distance and proper motion velocities are systematically varied following Kirihara et al. (2017b). To find the acceptable ranges of orbital parameters, we conduct a χ^2_{ν} analysis for the observed position of the NW Stream (see table 1 of Kirihara et al. 2017b) and radial velocities of the 5 GCs. Successful orbits satisfy the 1σ confidence level for the both criteria and have experienced two or more apocentric passages within 12 Gyr. We also use the NW Stream distance obtained from RC for Stream 1-4. Additional constraints in the test-particle simulations are (1) the test-particle passes within 0.5° from the center of each field and (2) the distance matches the observation within the observed uncertainty. Although the distance data derived by RC for Stream 1-4 have rather large errors, they give a strong constraint on potential orbits for the progenitor of the NW Stream as shown in Figure 16, and the number of allowable orbits is 3,290 in 5,068,617 orbit models.

The pericentric distance of the progenitor's orbit is one of the great keys to limit the physical properties of the progenitor. Figure 16a shows the number distribution of the successful orbits as a function of pericentric radius. The histogram has a peak between a pericentric distance of 20 kpc and 30 kpc. It is clear that no orbit can approach M31's center within 17 kpc. Even if we adopt the constraint for 3σ confidence level, any orbit cannot reach 17 kpc from the M31's center. The result provides an update criteria for the physical properties of the progenitor model. Following Kirihara et al. (2017b), we estimate the stripped mass of a progenitor using Hill radius at the pericenter that defines the tidal radius of the satellite in a gravitational potential of the host system. The half-light radius of the progenitor should be greater than 200 pc.

We demonstrate the formation process of the NW Stream using an N -body simulation. We construct the progenitor dwarf galaxy as a Plummer model using the MAGI (Miki & Umemura in prep.). The total mass M_{tot} and scale radius r_s of the Plummer distribution are set to $M_{\text{tot}} = 5 \times 10^7 M_{\odot}$ and $r_s = 1 \text{ kpc}$, respectively. The total number of particles is 65,536, and we use the gravitational octree code GOTHIC (Miki & Umemura 2017) to run the simulation. We adopt the Plummer softening parameter of 16 pc and the accuracy control parameter of 2^{-7} . The initial phase-space coordinates of the progenitor for the successful orbit are $(\xi, \eta, d, V_{\xi}, V_{\eta}, V_{\text{los}}) = (-22^{\circ}.18, -0^{\circ}.60, 860.07 \text{ kpc}, -9.88, -23.37, -302.15)$. The unit of velocity is km s^{-1} . In this model, the progenitor travels from north to south along the NW Stream with a perigalactic distance of 25.65 kpc. This demonstration is an updated version of their Case A simulation (see Figure 4 of Kirihara et al. 2017b).

Figure 16 shows an example of the N -body simulation of the NW Stream with our distance measurement, demonstrating that the simulation well represents the observation. To draw the distance distribution of the simulated NW Stream, we use the distribution of $\xi < 0$ on the sky. Together with the results for GCs, our observation strongly supports their simulation with the NW Stream as a background of M31. On the other hand, the latest PAndAS view (Richardson et al. 2011) suggests that the extension of the NW Stream is not clearly seen in their Figure 1 and may diminish or disappear when it passes the pericenter. This view is consistent with the case B simulation of Kirihara et al. (2017b). Therefore, the search for the southern extension of the NW Stream is important. Also, additional observation in the further northern field is important because the simulated stream extends outside of the PAndAS field. Future fine-tuning of the simulation is planned to derive more accurate properties of the NW Stream (Kirihara

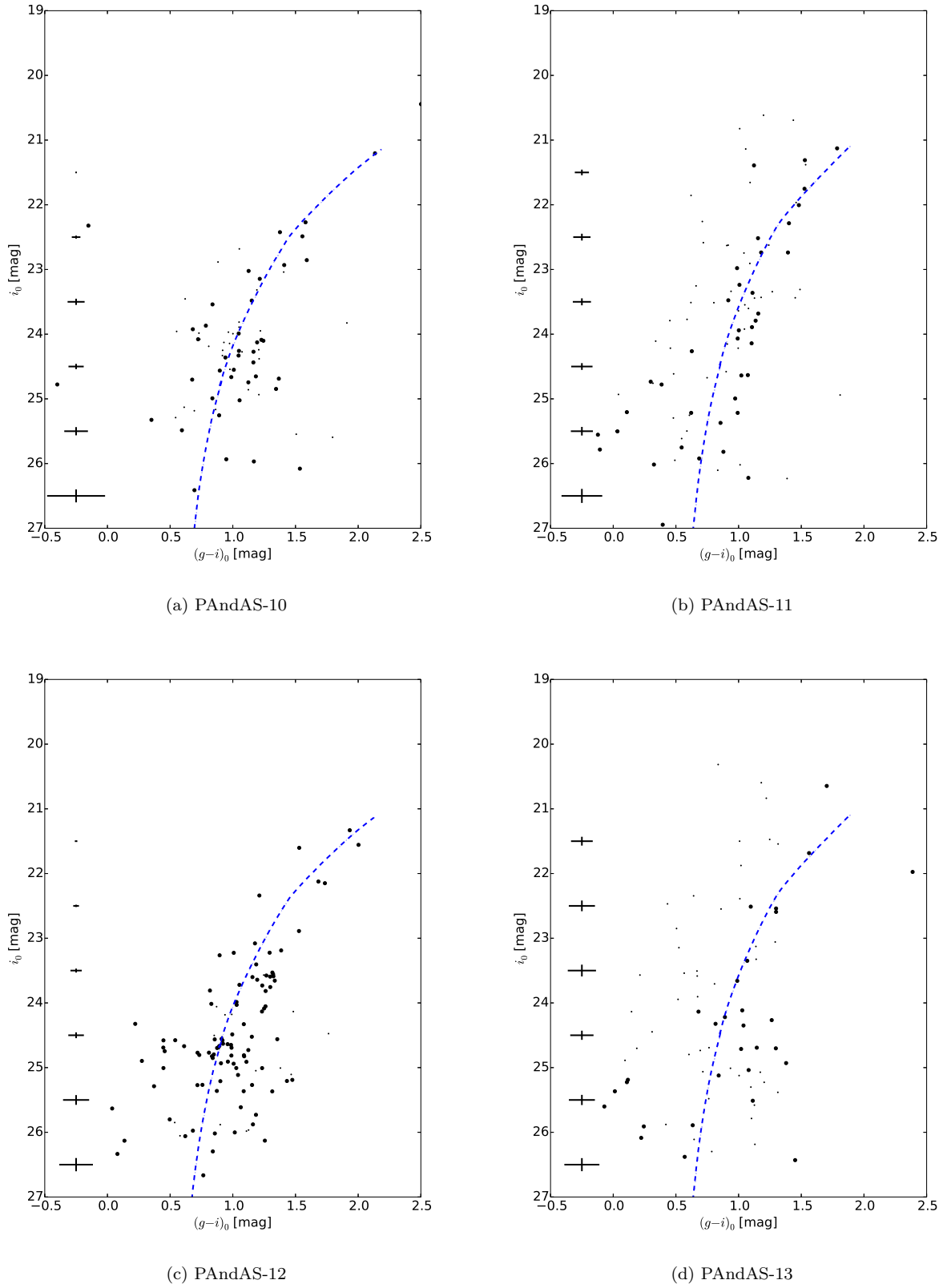


FIG. 14.— CMDs of GCs found on the NW Stream; (a) PAndAS-10, (b) PAndAS-11, (c) PAndAS-12 and (d) PAndAS-13. Large and small dots represent those stars with $Sharpness < 1$ and > 1 , respectively. The mean errors are calculated for every 1 mag and plotted as black crosses. Isochrone of RGB part with $(\log \tau_{\text{age}}, Z) = (10.12, 0.002)$, $(10.00, 0.001)$, $(10.00, 0.002)$ and $(10.12, 0.001)$ is overlaid for PAndAS-10 to 13, respectively. The distance modulus of $(m-M)=24.63$ is adopted.

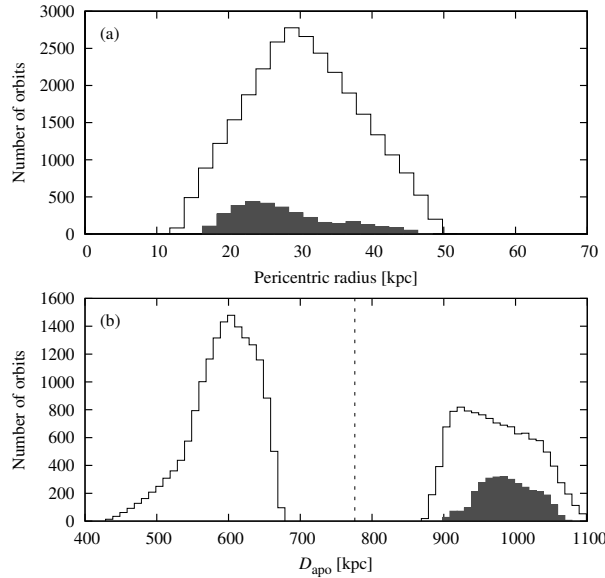


FIG. 15.— Histogram of (a) the pericentric radii and (b) the apocenter D_{apo} of the potential orbits. The thin lines indicate the possible orbits basically derived by Kiriwara et al. (2017b). The shaded area corresponds to the new orbits derived by this work including the observed distance of the NW Stream. The vertical dashed line in panel (c) marks the distance to M31 from Earth.

et al. in preparation). The key parameters from our survey are,

- The luminosity distribution along the stream: According to Kiriwara et al. (2017b), the N -body simulation can reproduce the observed features (i.e., the position of the NW Stream and the radial velocities for 5 GCs) for several Myr to 1 Gyr and it is difficult to determine the ‘current time’ during the orbital motion of the NW Stream in the halo of M31. The promising information to solve this degeneracy is the luminosity distribution along the stream. The reason that the simulated NW Stream has a higher surface brightness near the GC PAndAS-12 than other portions. This trend is attributed to the selection of the ‘current time’. Moreover, the position of the surviving central core of the progenitor gives strong constraint because it depends on the properties and orbit of the progenitor (Kiriwara et al. 2017b). As shown in Figures 7 and 13, our data provide a sufficient information and would be helpful to reveal the nature of the NW Stream.
- The width of the stream: As shown in Figure 15, the number of potential orbits of the NW Stream is still over several thousands although it is significantly reduced by making use of the line-of-sight distance to the stream. Therefore, other information to further constrain the orbits is required. By incorporating the width of the stream, the test-particle simulations will further constrain the allowable orbits. Figure 12 will be used for this purpose.

In relation to above, it is emphasized that the further observation along the NW Stream to both North and South directions be important. If the faint end of the stream is observed at the North as suggested from the PAndAS map, it will be a very strong constraint. The observation in short exposure mode with NB515 filter is effective to answer the question.

5.3. Diffuse Substructure

The surface brightness of RC stars found at the diffuse substructure ranges from 34.8 to 36 mag arcsec $^{-2}$ in g band (the median and brightest part is 35.5 and 34.8 mag arcsec $^{-2}$, respectively). The total surface brightness of the diffuse substructure can be estimated from that of RC stars assuming the isochrone and initial mass function (IMF). The offset between the total surface brightness and the surface brightness of RC stars is calculated to 1.69 mag in g band for $Z = 0.0014$ and $\log \tau_{\text{age}}(\text{Gyr}) = 10.00$ population with the Salpeter IMF. Therefore, the diffuse substructure would be observed as 33.1 – 34.3 mag arcsec $^{-2}$.

The surface brightness of 33 mag arcsec $^{-2}$ is below the detection limit of the previous surveys based on the resolved stellar photometry such as PAndAS and Tanaka et al. (2010). Our result clearly shows that RC stars can be a powerful probe of the diffuse substructures down to ~ 33 mag arcsec $^{-2}$. Since the number of substructures is predicted to increase as the surface brightness goes faint (e.g., Bullock & Johnston 2005), the actual appearance of the halo structure would be revealed in detail by tracing the RC stars. Only recently, the existence of an ultra-faint shell, having the common origin with the progenitor dwarf galaxy of the Giant Southern Stream, was predicted in the north-western area of M31 (Kiriwara et al. 2017a). The faint shell has similar properties with those of the diffuse substructure (surface brightness, distance and metallicity) while there is a spatial offset of around 2 deg. It suggests that the diffuse substructures may be remnants of past galactic mergers. We therefore emphasize that photometric surveys down to the RC magnitude are very important to understand the assembly process of many subsystems occurred in the outer part of the galaxy and to test the galaxy formation scenarios.

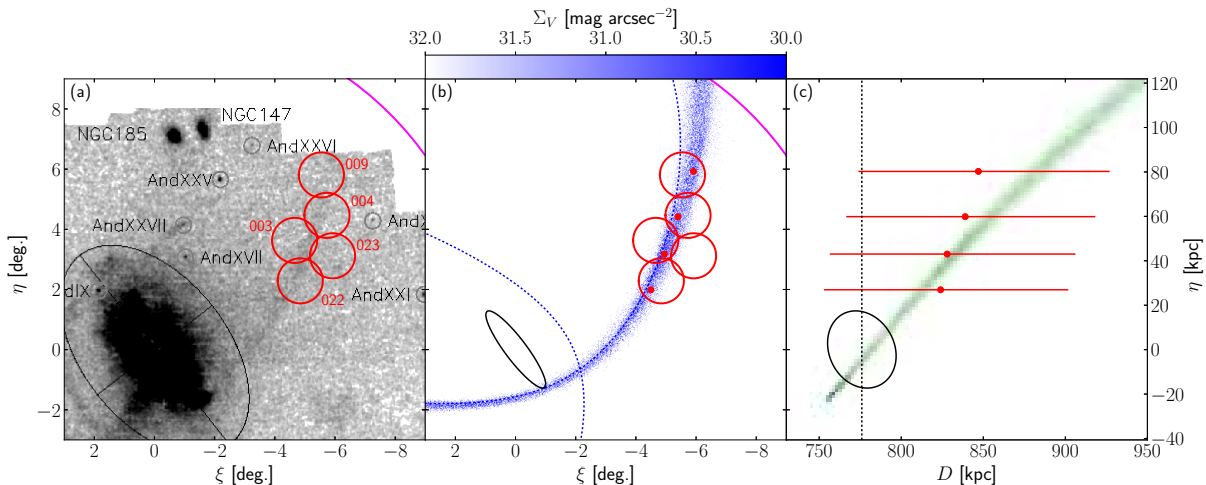


FIG. 16.— The 3D schematic picture of the NW Stream. The optical image is shown in panel (a), which is the same as Fig. 1. Particle distribution in panels (b) and (c) is a result of the N -body simulation. M31 is represented as an ellipse whose major diameter is 190 arcmin assuming inclination and position angle of 77° and 37° (Geehan et al. 2006), respectively. The HSC pointings are shown by red circles in panel (b). The magenta curve presents 150 kpc from the M31 center. The vertical black dashed line in panel (c) represents the distance to M31. The positions and distances of the Stream 1 to 4 are shown in red squares together with the error bars.

6. CONCLUSIONS

We have carried out a wide and deep imaging survey of the northwest part of the halo in M31 using HSC on the Subaru Telescope. The survey covers 9.2 deg^2 field consisting of 5 HSC pointings in g and i bands as well as a narrow band filter $NB515$. The reduced images in g , i and $NB515$ bands are deep enough with the mean 50% completeness limit of 26.31, 25.69 and 24.71 mag, respectively. The extinction corrected CMD of our survey field exhibits characteristic features; a band of dwarf stars of the MW disk, a narrow sequence of a diffuse stellar stream in the MW halo, the broad sequence consisting of the RGB stars in the M31 halo, a diffuse but distinct concentration of BHB stars, and a significant RC feature.

The spatial distribution of RC stars shows a prominent stream feature, which is the known NW Stream. This substructure is also confirmed in the spatial distribution of RGB stars in the M31 halo, which are selected using the $NB515$ photometry. The method using the tip of RGB is applied to the $NB515$ -selected RGB stars. We obtain the distance modulus to the NW Stream based on the TRGB method to be $24.42 \pm 0.033(\text{random}) \pm 0.033(\text{systematic})$ mag, but the isochrone fitting to the CMD of the Stream North suggests a larger distance modulus by 0.2-0.3 mag. The distance estimates by RC method show the distance moduli to be $24.63 \pm 0.191(\text{random}) \pm 0.057(\text{systematic})$ and $24.29 \pm 0.211(\text{random}) \pm 0.057(\text{systematic})$ mag for the Stream North and Off-Stream South, respectively, indicating that the NW Stream is located behind the main body of M31, whereas the diffuse substructure is located in front of M31. We also estimate the line-of-sight distances along the NW Stream and find that the south part of the NW Stream is ~ 20 kpc closer to us relative to the north part. The number density distribution across the NW Stream represented by RC stars is found to be fitted by a Gaussian with FWHM of ~ 25 arcmin, but slightly skewed to the south-west side. The number density distribution of RC stars along the NW Stream shows the complicated structure including the number of bumps and dips and a significant gap.

The stellar populations of globular clusters found on the NW Stream, PAndAS 10-13, are investigated based on the CMDs and they are suggested to be similar to that consisting of the NW Stream. The 3D structure of the NW Stream revealed in this study is compared with the recent simulation carried out by Kirihara et al. (2017a), and gives a definite constraint on the allowable orbit of the NW Stream. The surface brightness of the diffuse substructure found in the south part of the survey field is estimated to be $\sim 33 \text{ mag arcsec}^{-2}$ in g band, which is below the detection limit of the previous surveys of the M31 halo. We have found that the RC stars are a powerful probe to assess the diffuse substructures which are expected to be numerous and reveal the real appearance of the M31 halo.

This work is supported in part by JSPS Grant-in-Aid for Scientific Research (No. JP25287062, JP15K05037, JP25800098, JP25400222 and JP17H01101), MEXT Grant-in-Aid for Scientific Research on Innovative Areas (No. JP15H05892, JP16H01090 for K.H., for JP16H01086 for M.C.) and Grant-in-Aid for JSPS Fellows (T.K. 26.348). PG was supported by NSF grant AST-1412648. MGL and ISJ were supported by the National Research Foundation (NRF) grant funded by the Korea Government (NRF-2017R1A2B4004632).

We would like to thank all the staff of Subaru Telescope, in particular Drs. Fumiaki Nakata, Tsuyoshi Terai, Shintaro Koshida, Francois Finet, Akito Tajitsu, for their excellent support during the observation, and all the staff of HSC software developing group, in particular Dr. Hisanori Furusawa and Dr. Naoki Yasuda, for their advice during the processing of our M31 data. We would like to express our appreciation to Dr. Satoshi Kawanomoto for his effort in developing NB515 filter. We are grateful to Dr. Paul Price for his kind support to calibrate our data to the PS1 system. We appreciate many valuable comments and suggestions from the referee which have improved this paper significantly.

The numerical computations were carried out on the HA-PACS System in the Center for Computational Sciences, University of Tsukuba, Japan.

The Hyper Suprime-Cam (HSC) collaboration includes the astronomical communities of Japan and Taiwan, and Princeton University. The HSC instrumentation and software were developed by the National Astronomical Observatory of Japan (NAOJ), the Kavli Institute for the Physics and Mathematics of the Universe (Kavli IPMU), the University of Tokyo, the High Energy Accelerator Research Organization (KEK), the Academia Sinica Institute for Astronomy and Astrophysics in Taiwan (ASIAA), and Princeton University. Funding was contributed by the FIRST program from Japanese Cabinet Office, the Ministry of Education, Culture, Sports, Science and Technology (MEXT), the Japan Society for the Promotion of Science (JSPS), Japan Science and Technology Agency (JST), the Toray Science Foundation, NAOJ, Kavli IPMU, KEK, ASIAA, and Princeton University. This paper makes use of software developed for the Large Synoptic Survey Telescope. We thank the LSST Project for making their code freely available. The Pan-STARRS1 (PS1) Surveys have been made possible through contributions of the Institute for Astronomy, the University of Hawaii, the Pan-STARRS Project Office, the Max-Planck Society and its participating institutes, the Max Planck Institute for Astronomy and the Max Planck Institute for Extraterrestrial Physics, The Johns Hopkins University, Durham University, the University of Edinburgh, Queen's University Belfast, the Harvard-Smithsonian Center for Astrophysics, the Las Cumbres Observatory Global Telescope Network Incorporated, the National Central University of Taiwan, the Space Telescope Science Institute, the National Aeronautics and Space Administration under Grant No. NNX08AR22G issued through the Planetary Science Division of the NASA Science Mission Directorate, the National Science Foundation under Grant No. AST-1238877, the University of Maryland, and Eotvos Lorand University (ELTE).

APPENDIX

TRANSFORMATION BETWEEN THE HSC AND OTHER STANDARD PHOTOMETRIC SYSTEMS

Photometric transformations are required to compare our results with previous studies which were carried out in different filter systems. In this section, the color conversion formulae which are relevant to our study are summarized. The method to obtain the formulae is similar to those used in previous studies such as Yagi et al. (2010) and Fukugita et al. (1995). We calculate the colors of stars using the Bruzual-Persson-Gunn-Stryker (BPGS) Atlas by convolving the transmission curve of a filter system [Johnson-Cousins system for Bessell (1990) and SDSS system for Doi et al. (2010)] to the stellar spectra. The transmission curves for HSC can be obtained from the Subaru Telescope HSC website.²⁴

Figure 17 shows our calculation. The top panel of each of the figure sections (a)–(d) shows the calculated colors ($V - I_C$, $i_{HSC} - I_C$, $B - V$, $g_{HSC} - V$) for BPGS stars plotted against $(g - i)_{HSC}$. The best-fit functions, linear expression and quadratic expression, are plotted as green and cyan dashed lines, respectively. The fitting to the quadratic expression is performed for $-0.5 < (g - i)_{HSC} < 2.0$, but that to the linear expression is for a more limited color range ($1.3 < (g - i)_{HSC} < 1.7$) which is relevant to this study. In the middle and bottom panels, the residuals from the quadratic and linear fits, respectively, are plotted against $(g - i)_{HSC}$.

The fitting for $i_{HSC} - I_C$ is performed very well with root mean square (RMS) residuals of 0.008–0.009 and those for $g_{HSC} - V$ and $V - I_C$ are fair with an RMS of ~ 0.019 . That for $B - V$ is the worst but the RMS is reasonable if the color range is limited to $0.4 < (g - i)_{HSC} < 1.2$ which is sufficient for this study. In this study, we use

$$V - I_C = 0.715(g - i)_{HSC} + 0.317 \quad \text{for } 1.3 < (g - i)_{HSC} < 1.7, \quad (\text{A1})$$

$$i_{HSC} - I_C = 0.067(g - i)_{HSC} + 0.426, \quad (\text{A2})$$

$$B - V = 0.709(g - i)_{HSC} + 0.170 \quad \text{for } 0.4 < (g - i)_{HSC} < 1.2, \quad (\text{A3})$$

$$g_{HSC} - V = 0.371(g - i)_{HSC} + 0.068, \quad (\text{A4})$$

for the analysis.

We also use the color conversion formulae from the SDSS system to the HSC system,

$$i_{HSC} = i_{SDSS} + 0.00130204 - 0.16922042(i_{SDSS} - z_{SDSS}) - 0.01374245(i_{SDSS} - z_{SDSS})^2, \quad (\text{A5})$$

$$g_{HSC} = g_{SDSS} - 0.00816446 - 0.08366937(g_{SDSS} - r_{SDSS}) - 0.00726883(g_{SDSS} - r_{SDSS})^2, \quad (\text{A6})$$

which are adopted in hscPipe, when converting the isochrone described in the SDSS system. During the image reduction, the HSC images are calibrated against PS1 using the following color conversion formulae,

$$i_{HSC} = i_{PS1} + 0.00166891 - 0.13944659(i_{PS1} - z_{PS1}) - 0.03034094(i_{PS1} - z_{PS1})^2, \quad (\text{A7})$$

$$g_{HSC} = g_{PS1} + 0.00730066 + 0.06508481(g_{PS1} - r_{PS1}) - 0.0151057(g_{PS1} - r_{PS1})^2, \quad (\text{A8})$$

The top panels of the four sections (a)–(d) of Figure 18 show the magnitude difference between HSC and either SDSS or PS1 systems of g and i band (i.e., color terms) calculated for BPGS stars as a function of color. These panels indicate that the magnitude difference can be represented as quadratic expressions of color for wide color ranges. The bottom panels of the four sections (a)–(d) of Figure 18 show the difference between HSC magnitude and that

²⁴ <http://www.naoj.org/Observing/Instruments/HSC/index.html>

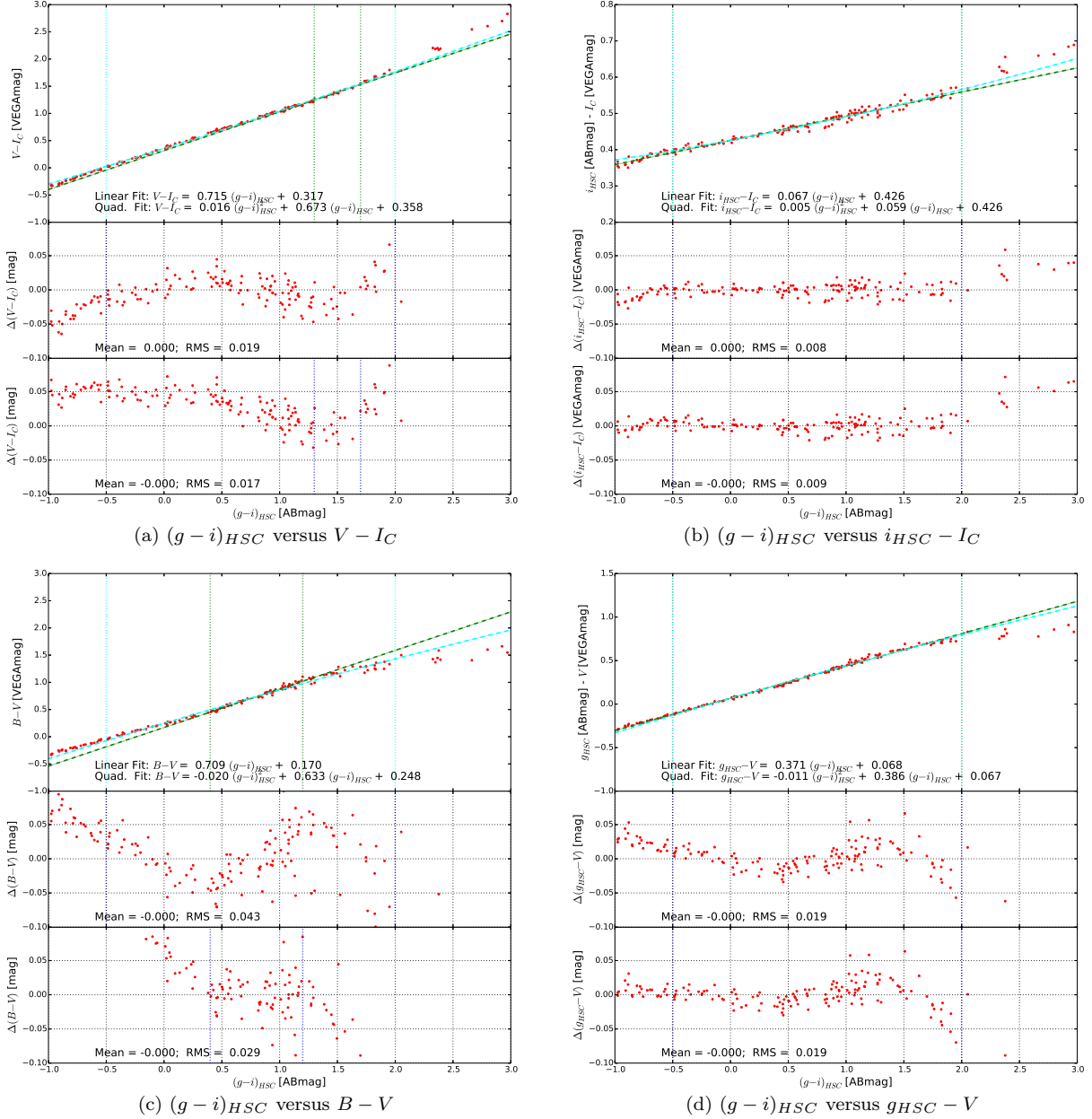


FIG. 17.— Color conversion diagrams between (a) $(g-i)_{HSC}$ and $V-I_C$, (b) $(g-i)_{HSC}$ and $i_{HSC}-I_C$, (c) $(g-i)_{HSC}$ and $B-V$, and (d) $(g-i)_{HSC}$ and $g_{HSC}-V$. For each of the parts (a)–(d): (Top) The calculated colors for BPGS stars are plotted against $(g-i)_{HSC}$. The best-fit functions, linear expression and quadratic expression, are plotted as green and cyan dashed lines and the color range used for the fitting is plotted as vertical dotted lines with same color, respectively. (Middle) The residuals of calculated color from the quadratic fit. The blue vertical dotted lines indicate the color range used for the fitting. (Bottom) Same as for the middle panel, but for the linear fit.

calculated using equations A5–A8. The RMS is calculated for stars with moderate color [i.e., $(g-r)_{SDSS,PS1} < 2.0$ or $(i-z)_{SDSS,PS1} < 1.0$] and found to be less than 0.01 mag.

REFERENCES

- Alvez, D. R. & Sarajedini, A. 1999, *ApJ*, 511, 225
 Belokurov, V., Zucker, D. B., Evans, N. W., et al. 2006, *ApJ*, 642, L137
 Bessell, M. S. 1990, *PASP*, 102, 1181
 Bilir, S., Ak, T., Ak, S., Yontan, T. & Bostanci, Z. F. 2013, *NewA*, 23, 88
 Bosch, J., Armstrong, R., Bickerton, S., et al. 2017, [arXiv:1705.06766](https://arxiv.org/abs/1705.06766)
 Bressan, A., Marigo, P., Girardi, L., et al. 2012, *MNRAS*, 427, 127
 Bullock, J. S., & Johnston, K. V. 2005, *ApJ*, 635, 931
 Carlberg, R. G., Richer, H. R., McConnachie, A. W., et al. 2011, *ApJ*, 731, 124
 Carlberg, R. G. 2012, *ApJ*, 748, 20
 Castelli, F., & Kurucz, R. L. 2004, [arXiv:astro-ph/0405087](https://arxiv.org/abs/astro-ph/0405087)
 Chabrier, G. 2001, *ApJ*, 554, 1274
 Conn, A. R., Lewis, G. F., Ibata, R. A., et al. 2011, *ApJ*, 740, 69
 Cooper, A. P., Cole, S., Frenk, C. S., et al. 2010, *MNRAS*, 406, 744
 Doi, M., Tanaka, M., Fukugita, M., et al. 2010, *AJ*, 139, 1628
 Drlica-Wagner, A., Bechtol, K., Rykoff, E. S., et al. 2015, *ApJ*, 813, 109

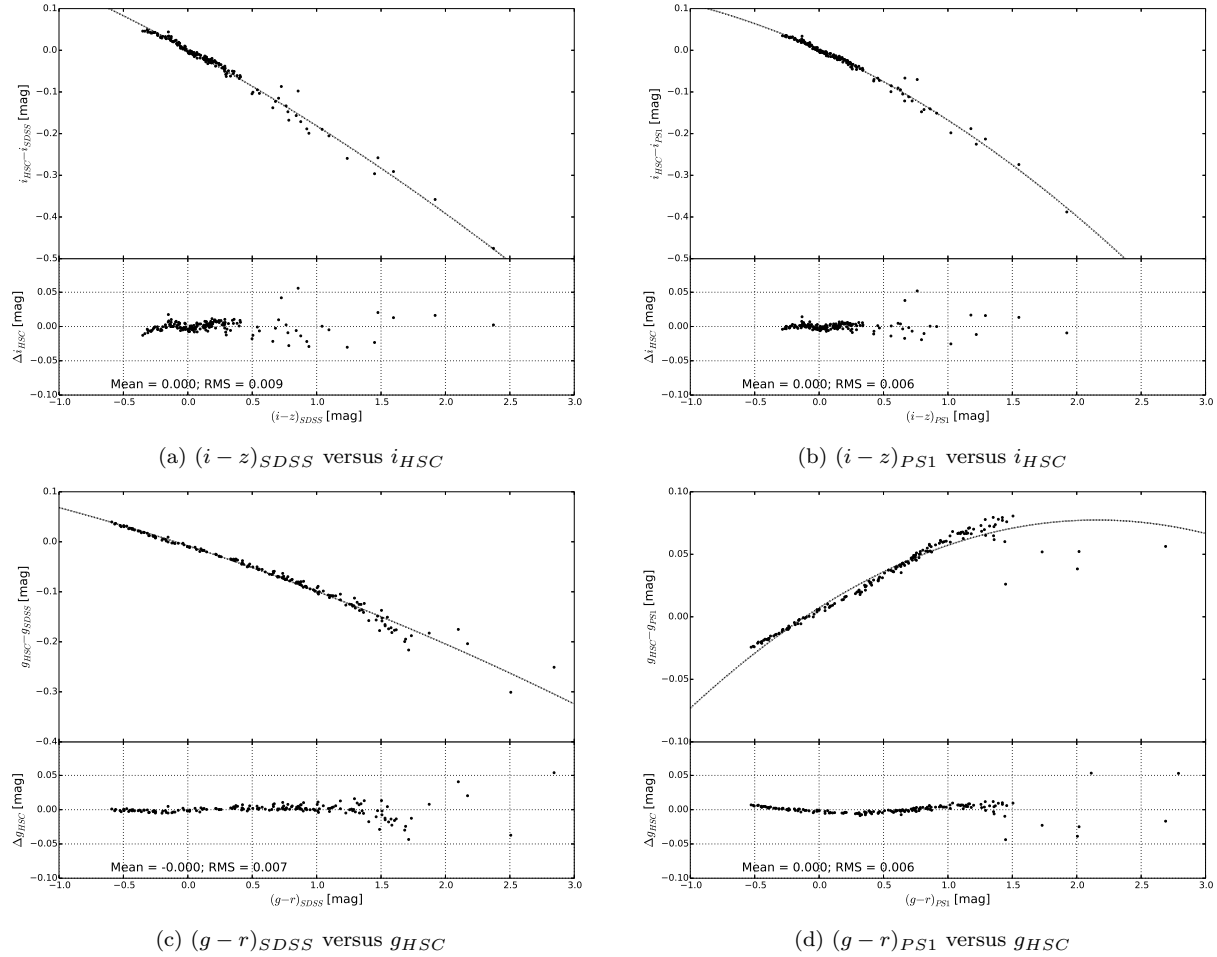


FIG. 18.— Color conversion diagrams between (a) $(i-z)_{SDSS}$ and i_{HSC} , (b) $(i-z)_{PS1}$ and i_{HSC} , (c) $(g-r)_{SDSS}$ and g_{HSC} , and (d) $(g-r)_{PS1}$ and g_{HSC} . For each of the parts (a)–(d): (Top) The magnitude difference between HSC and either SDSS or PS1 systems of g and i band (i.e., color terms) calculated for BPGS stars as a function of color. The dotted line shows the quadratic expression of the data, which is one of equations A5–A8. (Bottom) The magnitude difference between HSC magnitude and that calculated with one of equations A5–A8. The RMS value is calculated for stars with moderate color [i.e., $(g-r)_{SDSS,PS1} < 2.0$ or $(i-z)_{SDSS,PS1} < 1.0$] and listed in the figure.

Erkal, D., Belokurov, V., Bovy, J., & Sanders, J. L. 2016, MNRAS, 463, 102

Fardal, M. A., Guhathakurta, P., Babul, A., & McConnachie, A. W. 2007, MNRAS, 380, 15

Feltzing, S., & Chiba, M. 2013, New Astronomy Rev., 57, 80

Font, A. S., McCarthy, I. G., Crain, R. A., et al. 2011, MNRAS, 416, 2802

Fukugita, M., Shimasaku, K., & Ichikawa, T. 1995, PASP, 107, 945

Furusawa, H., Koike, M., Takata, T. et al. 2017, PASJ, in press (doi: 10.1093/pasj/psx079)

Geehan, J. J., Fardal, M. A., Babul, A., & Guhathakurta, P. 2006, MNRAS, 366, 996

Gilbert, K. M., Guhathakurta, P., Kalirai, J. S., et al. 2006, ApJ, 652, 1188

Gilbert, K. M., Guhathakurta, P., Beaton, R. L., et al. 2012, ApJ, 760, 76

Gilbert, K. M., Kalirai, J. S., Guhathakurta, P., et al. 2014, ApJ, 796, 76

Gilmore, G., Wilkinson, M. I., Wyse, R. F. G., et al. 2007, ApJ, 663, 948

Guhathakurta, P., Ostheimer, J. C., Gilbert, K. M., et al. 2005, arXiv:astro-ph/0502366

Gunn, J. E., & Stryker, L. L. 1983, ApJS, 52, 121

Harris, W. E. 1996, AJ, 112, 1487

Hernquist, L. 1990, ApJ, 356, 359

Huxor, A. P., Mackey, A. D., Ferguson, A. M. N. et al. 2014, MNRAS, 442, 2165

Ibata, R. A., Lewis, G. F., Conn, A. R., et al. 2013, Nature, 493, 62

Ibata, R. A., Lewis, G. F., McConnachie, A. W., et al. 2014, ApJ, 780, 128

Ivezic, Z., Axelrod, T., Brandt, W. N., et al. 2008, AJ, 176, 1

Jang, I. S., & Lee, M. G. 2017, ApJ, 835, 28

Jester, S., Schneider, D. P., Richards, G. T., et al. 2005, AJ, 130, 873

Juric, M., Ivezic, Z., Brooks, A., et al. 2008, ApJ, 673, 864

Juric, M., Kantor, J., Lim, K.-T., et al. 2015, ArXiv e-prints, arXiv:1512.07914

Kalirai, J. S., Gilbert, K. M., Guhathakurta, P., et al. 2006, ApJ, 648, 389

Kawanomoto, S., Uruguchi, F., Komiyama, Y. et al. 2017, PASJ, in press

Kirihara, T., Miki, Y., Mori, M., Kawaguchi, T., & Rich, R. M. 2017a, MNRAS, 464, 3509

Kirihara, T., Miki, Y., & Mori, M. 2017b, MNRAS, 469, 3390

Komiyama, Y., Obuchi, Y., Nakaya, H. et al. 2017, PASJ, in press (doi: 10.1093/pasj/psx069)

Koposov, S., Belokurov, V., Evans, N. W., et al. 2008, ApJ, 686, 279

Koposov, S. E., Belokurov, V., Torrealba, G., & Evans, N. W. et al. 2015, ApJ, 805, 130

Kroupa, P. 2002, Science, 295, 82

Küpper, A. H. W., Lane, R. R., & Heggie, D. C. 2012, MNRAS, 420, 2700

Macciò, A. V., & Fontanot, F. 2010, MNRAS, 404, L16

- Magnier, E. A., Schlafly, E., Finkbeiner, D., et al. 2013, *ApJS*, 205, 20
- Majewski, S. R., Ostheimer, J. C., Kunkel, W. E., & Patterson, R. J. 2000, *AJ*, 120, 2550
- Martin, N. F., de Jong, J. T. A., Rix, H.-W. et al. 2008, *ApJ*, 684, 1075
- Martin, N. F., Ibata, R. A., Rich, R. M. et al. 2014, *ApJ*, 787, 19
- McConnachie, A. W., Irwin, M. J., Ibata, R. A. et al. 2009, *Nature*, 461, 66
- McConnachie, A. W. 2012, *AJ*, 144, 4
- Miki, T. & Umemura, M. 2017, *New Astronomy*, 52, 65
- Miyazaki, S., Komiyama, Y., Nakaya, H. et al. 2012, *Proc. SPIE*, 8446, 84460Z
- Miyazaki, S., Komiyama, Y., Kawanomoto, S. et al. 2017, *PASJ*, in press (doi: 10.1093/pasj/psx063)
- Morrison, H. L., Mateo, M., Olszewski, E. W., Harding, P., Dohm-Palmer, R. C., Freeman, K. C., Norris, J. E., & Morita, M. 2000, *AJ*, 119, 2254
- Navarro, J. F., Frenk, C. S. & White, S. D. M. 1998, *ApJ*, 462, 563
- Pickles, A. J. 1998, *PASP*, 110, 863
- Richardson, J. C., Irwin, M. J., McConnachie, A. W. et al. 2011, *ApJ*, 732, 76
- Rizzi, L., Tully, R. B., Makarov, D., et al. 2007, *ApJ*, 661, 815
- Sakai, S., Madore, B. F. & Freedman, W. L. 1996, *ApJ*, 461, 713
- Sakamoto, T., & Hasegawa, T. 2006, *ApJ*, 653, L29
- Salpeter, E. E. 1955, *ApJ*, 121, 161
- Sawala, T., Frenk, C. S., & Fattahi, A. et al. 2016, *MNRAS*, 457, 1931
- Schlafly, E. F., & Finkbeiner, D. P. 2011, *ApJ*, 737, 103
- Schlafly, E. F., Finkbeiner, D. P., Jurić, M. et al. 2012, *ApJ*, 756, 158
- Schlegel, D. J., Finkbeiner, D. P., & Davis, M. 1998, *ApJ*, 500, 525
- Simon, J. D., & Geha, M. 2007, *ApJ*, 670, 313
- Stetson, P. B. 1987, *PASP*, 99, 191
- Stetson, P. B. 1994, *PASP*, 106, 250
- Tanaka, M., Chiba, M., Komiyama, Y., Guhathakurta, P., Kalirai, J. S., & Iye, M. 2010, *ApJ*, 708, 1168
- Tanaka, M., Chiba, M., & Komiyama, Y. 2017, *ApJ*, 842, 127
- Tollerud, E. J., Bullock, J. S., Strigari, L. E., & Willman, B. 2008, *ApJ*, 688, 277
- Tollerud, E. J., Geha, M. C., Grcevich, J., Putman, M. E., Weisz, D. R., & Dolphin, A. E. 2016, *ApJ*, 827, 89
- Tonry, J. L., Stubbs, C. W., Lykke, K. R. et al. 2012, *ApJ*, 750, 99
- Veljanoski, J., Mackey, A. D., Ferguson, A. M. N. et al. 2014, *MNRAS*, 442, 2929
- Walsh, S. M., Willman, B., & Jerjen, H. 2009, *AJ*, 137, 45
- Willman, B., Blanton, M. R., West, A. A., et al. 2005, *AJ*, 129, 2692
- Yagi, M., Yoshida, M., Komiyama, Y., et al. 2010, *AJ*, 140, 1814
- York, D. G., Adelman, J., Anderson, J. E. Jr., et al. 2000, *AJ*, 120, 1579